

The GALEX-PTF experiment: II. supernova progenitor radius and energetics via shock-cooling modeling

NOAM GANOT,¹ ERAN O. OFEK,¹ AVISHAY GAL-YAM,¹ MAAYANE T. SOUMAGNAC,^{2,1} JONATHAN MORAG,¹ ELI WAXMAN,¹ SHRINIVAS R. KULKARNI,³ MANSI M. KASLIWAL,⁴ AND JAMES NEILL⁴

¹*Department of Particle Physics and Astrophysics, Faculty of Physics, The Weizmann Institute of Science, Rehovot 76100, Israel*

²*Lawrence Berkeley National Laboratory, 1 Cyclotron Road, Berkeley, CA 94720, USA*

³*Cahill Center for Astrophysics, California Institute of Technology, 1200 E. California Boulevard, Pasadena, CA 91125, USA*

⁴*Division of Physics, Mathematics, and Astronomy, California Institute of Technology, Pasadena, CA 91125, USA*

ABSTRACT

The radius and surface composition of an exploding massive star, as well as the explosion energy per unit mass, can be measured using early ultraviolet (UV) observations of core-collapse supernovae (CC SNe). We present the results from a simultaneous GALEX and Palomar Transient Factory (PTF) search for early UV emission from SNe. We analyze five CC SNe for which we obtained *NUV* measurements before the first ground-based *R*-band detection. We introduce SOPRANOS, a new maximum likelihood fitting tool for models with variable temporal validity windows, and use it to fit the Sapir & Waxman (2017) shock cooling model to the data. We report four Type II SNe with progenitor radii in the range of $R_* \approx 600 - 1100 R_\odot$ and a shock velocity parameter in the range of $v_{s*} \approx 2700 - 6000 \text{ km s}^{-1}$ ($E/M \approx 2 - 8 \times 10^{50} \text{ erg/M}_\odot$) and one type IIb SN with $R_* \approx 210 R_\odot$ and $v_{s*} \approx 11000 \text{ km s}^{-1}$ ($E/M \approx 1.8 \times 10^{51} \text{ erg/M}_\odot$). Our pilot GALEX/PTF project thus suggests that a dedicated, systematic SN survey in the *NUV* band, such as the wide-field UV explorer *ULTRASAT* mission, is a compelling method to study the properties of SN progenitors and SN energetics.

Keywords: supernovae: general; Astrophysics - High Energy Astrophysical Phenomena; Astrophysics - Cosmology and Nongalactic Astrophysics

1. INTRODUCTION

A Core collapse Supernova (SN) explosion marks the end of life of a massive star. Although there is a wide range of evidence to support this, the details of the final stages of the evolution of such massive stars (see, e.g. Langer 2012, and references within) and the exact association between SN type and progenitor type are not firmly established (see reviews by Filippenko 1997; Smartt et al. 2009; Smartt 2015; Gal-Yam 2017).

Most previous, existing and planned SN surveys such as the Palomar Transient Factory (PTF; Law et al. 2009; Rau et al. 2009), the Large Synoptic Survey Telescope (LSST; Ivezić et al. 2019), the All Sky Automated Survey for Supernovae (ASAS SN; Shappee et al. 2014), the Asteroid Terrestrial-impact Last Alert System (ATLAS; Tonry et al. 2018), Large Array Survey Telescope (LAST; Ofek & Ben-Ami

2020) and the Zwicky Transient Facility (ZTF; Bellm 2014) are limited to the visible-NIR wavelengths. Only a few SNe were detected by space telescopes in shorter wavelengths, often by coincidence (e.g. Arnett et al. 1989; Schmidt et al. 1993; Camp et al. 2013; Gezari et al. 2008, 2010; Schawinski et al. 2008; Soderberg et al. 2008; Ofek et al. 2010; Arcavi et al. 2011; Gal-Yam et al. 2011; Cao et al. 2013; Soumagnac et al. 2020). Theoretical models predict that the earliest emission from CC SNe is a burst of radiation occurring when the explosion shock breaks out of the stellar surface (the shock breakout flare). This flare is expected to have temperatures in the range of few to tens of eV, and its duration would be R_*/c , where R_* is the stellar radius, i.e., a timescale of about 1 hour (Grassberg et al. 1971; Colgate 1974; Falk 1978; Klein & Chevalier 1978; Ensmann & Burrows 1992; Matzner & McKee 1999; Nakar & Sari 2010; Sapir et al. 2011; Katz et al. 2012; Sapir et al. 2013). At these temperatures, the UV emission is expected to be stronger than the one in the visible band. Following the break-

out flare the expanding stellar envelope enters a shock cooling phase where it emits a fraction of the leftover explosion energy. This phase is better understood theoretically (e.g., Grassberg et al. 1971; Chevalier 1976, 1992; Chevalier & Fransson 2008; Nakar & Sari 2010; Rabinak & Waxman 2011; Sapir & Waxman 2017). According to those models it takes a few days for the photospheric temperature to cool to temperatures below 1eV and for the peak flux to move into the visible band. Fortunately, there were a few SNe which had some early near UV (*NUV*) measurements (by *GALEX*, Gezari et al. 2008; Schawinski et al. 2008; and by Swift, Soderberg et al. 2008) which allowed to test these models at temperature $\gtrsim 1\text{eV}$. Rabinak & Waxman (2011) have demonstrated that early shock cooling phase data encodes information about the progenitor radius and surface composition, the SN explosion energy per unit mass and the line of sight extinction.

In a recent work, Goldberg & Bildsten (2020) point out that models that follow the evolution of SNe II-P during the plateau phase suffer from an inherent degeneracy in determining the properties of the progenitors. This emphasizes the importance of early data and models which are valid in those time to be able to determine the SN progenitor properties. In this paper we present the results of the first systematic space-borne *NUV* survey for SN and the fitting of the model of Sapir & Waxman (2017) to the observations. A more comprehensive and sensitive survey will be conducted with the launch of the *ULTRASAT* mission (Sagiv et al. 2014) expected by 2024.

We present our observations on §2, describe the Sapir & Waxman (2017) model and our SOPRANOS fitting formalism in §3, report our fit results in §4, discuss them in §5 and conclude in §6.

2. OBSERVATIONS

Between 2012 May 24 and 2012 July 28 we monitored about 600deg^2 of high galactic latitude sky using the *GALEX* satellite (Martin et al. 2005) and the Palomar Transient Factory (PTF; Law et al. 2009; Rau et al. 2009). The observations were conducted with the *GALEX-NUV* filter and the PTF Mould *R* band. This *GALEX*-PTF experiment is further described in Ganot et al. (2016). During the experiment ten core collapse Supernovae were detected in the PTF *R*-band observations. For six SNe out of the ten a matching transient was detected in the *GALEX NUV* observations. In this paper we analyze the light curves of the SNe detected in the experiment. The SNe detected are listed in Table 1 as appeared in Ganot et al. (2016).

2.1. *GALEX* data

During our experiment, *GALEX* (Martin et al. 2005) was operating in scanning mode¹ and its *NUV* camera (Morrissey et al. 2007) observed strips in the sky in a drift-scan mode with an effective average exposure time of about 80s, reaching a *NUV* 5σ limiting magnitude of 20.6 mag AB. Each strip was visited once every three days. The *GALEX NUV* photometry was measured using custom aperture photometry routines (Ofek 2014) and is described in details in Ganot et al. (2016). Some of the SNe appear in more than one strip sub-scan leading to two adjacent visits within the *GALEX* three day cadence. Some of the scans were lost due to failed down-link and image corruption leading to missing points on the light curves. The *GALEX* photometry observations are listed in Table 2, and plotted together with a shock cooling fit of each SN (see §4; Figs. 7, 11, 16, 20, 24).

2.2. PTF data

The Palomar Transient Factory (PTF), using the 48 inch Oschin Schmidt Telescope at Palomar Observatory equipped with a CCD mosaic, with a field of view of 7.26deg^2 , was scanning a similar sky patch as *GALEX* in its Mould *R*-band, reaching an *R*-band limiting magnitude of about 21 mag AB with a cadence of two days, weather permitting. During the experiment PTF discovered ten core collapse SNe, listed in Table 1. The photometry was extracted using a point-spread function (PSF) fitting routine (Sullivan et al. 2006; Firth et al. 2015) applied after image subtraction that was done using the Alard & Lupton (1998) algorithm. The PTF data reduction is described in Laher et al. (2014), while the photometric calibration and magnitude system are described by Ofek et al. (2012). The PTF photometry observations are listed in Table 3, and plotted with the SN individual fits (see §4; Figs. 7, 11, 16, 20 and 24).

2.3. Spectra

Following the PTF transient detection several spectra were taken using the Keck I 10 m telescope Low Resolution Imaging Spectrometer (LRIS; Oke et al. 1995), the Keck II 10 m telescope DEep Imaging Multi-Object Spectrograph (DEIMOS; Faber et al. 2003), the Apache Point Observatory 3.5 m telescope Dual Imaging Spectrograph², and DBSP, the Palomar 200-inch Hale telescope Double Beam Spectrograph³. The spectra are listed in Table 4 and shown in Figures 1, 2, 3, 4, 5 and 6. All observations are made public via WiseREP⁴

¹ <http://galex.stsci.edu/gr6/?page=scanmode>

² <http://www.apo.nmsu.edu/arc35m/Instruments/DIS/>

³ <http://www.astro.caltech.edu/palomar/observer/200inchResources/dbspov/>

⁴ <https://wiserep.weizmann.ac.il/>

Table 1. The core-collapse SNe detected by PTF during the GALEX/PTF experiment

PTF name	J2000 RA	J2000 Dec	Redshift	Type	PTF discovery date	E_{B-V}^a [mag]	NUV background [erg s ⁻¹ cm ⁻² Å ⁻¹]
PTF12ffs	14:42:07.33	+09:20:29.8	0.0511	SN II ^b	June 10, 2012	0.025	2.24×10^{-16}
PTF12fhz	15:18:20.09	+10:56:42.7	0.0987	SN IIb	June 12, 2012	0.038	6.09×10^{-18}
PTF12fkp	14:46:54.81	+10:31:26.4	0.12	SN II-L	June 14, 2012	0.026	1.45×10^{-17}
PTF12ftc	15:05:01.88	+20:05:54.6	0.0732	SN II-P	June 19, 2012	0.036	4.24×10^{-17}
PTF12glz	15:54:53.04	+03:32:07.5	0.0799	SN II _n	July 7, 2012	0.132	4.84×10^{-17}
PTF12gnt	17:27:47.30	+26:51:22.1	0.029	SN II-P	July 9, 2012	0.047	1.20×10^{-15}
PTF12fes	16:00:35.13	+15:41:03.5	0.0359	SN Ib	June 9, 2012	0.038	4.24×10^{-17}
PTF12fip	15:00:51.04	+09:20:25.1	0.034	SN II-P	June 12, 2012	0.030	4.66×10^{-16}
PTF12frn	16:22:00.16	+32:09:38.9	0.136	SN II _n	June 18, 2012	0.021	5.08×10^{-16}
PTF12gcx	15:44:17.32	+09:57:43.1	0.045	SN II ^c	June 26, 2012	0.054	5.18×10^{-16} ^d

For the four SNe below the line, no matching *NUV* transient was identified in the *GALEX* images.

^a The Galactic extinction according to [Schlegel et al. \(1998\)](#) maps.

^b A bright SN II with a light curve intermediate between SNe II-P and II-L

^c A bright SN II with a very long rise time, similar to SN 1998A ([Pastorello et al. 2005](#)), SN 2000cb ([Kleiser et al. 2011](#)) and SNe 2005ci and 2005dp ([Arcavi et al. 2012](#)). see also [Taddia et al. \(2015\)](#).

^d The PTF12gcx background was calculated using only *GALEX* data measurements prior to the SN detection by PTF, since the *NUV* transient could not be localized.

Table 2. PTF12ffs *GALEX* *NUV* data

MJD [days]	CPS ^a	CPSERR ^b	M_{AB}
56073.411	0.664	0.148	20.52
56073.412	1.214	0.166	19.87
56076.151	0.822	0.154	20.29
56076.151	1.267	0.180	19.82
56078.890	2.851	0.282	18.94
...			

The full *GALEX* data for the events reported in the paper is available in the electronic version.

^a counts s⁻¹

^b counts s⁻¹ 1 σ error

Table 3. PTF12ffs PTF *R* data

MJD [days]	counts	dcounts	zero point	M_{AB}
56077.192	-4.7	85.3	27.000	(21) ^a
56077.227	-117.9	75.0	27.000	(21.93) ^a
56077.257	35.8	74.4	27.000	23.12
56081.188	1126.8	198.5	27.000	19.37
56081.220	1262.9	216.6	27.000	19.25
...				

The full PTF data for the events reported in the paper is available in the electronic version.

^a Negative count values cannot be converted to magnitudes. Instead of magnitudes we report 3 σ limit magnitudes for these measurements.

([Yaron & Gal-Yam 2012](#)). All spectra include strong

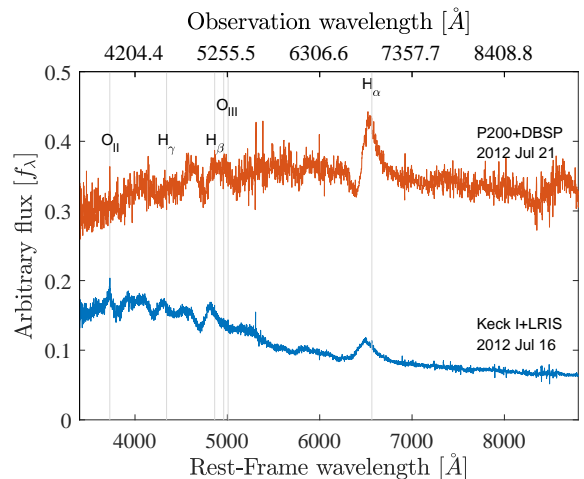


Figure 1. Spectra of PTF12ffs obtained from various observatories (see Table 4). We used H_{α} , H_{β} , H_{γ} , O_{II} and O_{III} common galaxy lines (plotted) to measure a red shift of 0.0511.

absorption lines indicating that the photosphere was already recombined at the epochs the spectra were taken.

3. ANALYSIS

We fit the observed *NUV* and *R*-band light curves with shock cooling models described in [Rabinak & Waxman \(2011, hereafter RW11\)](#) with the modifications of [Sapir & Waxman \(2017, hereafter SW17\)](#) and [Morag et al. \(2020, in prep., hereafter MSW20\)](#). All these models describe the shock cooling phase of a SN and do not treat the interaction between the SN radiation and a circumstellar mate-

Table 4. Spectroscopy measurement for GALEX/PTF SNe

SN name	Telescope	Instrument	Date
PTF12ffs	Keck I	LRIS	2012 Jun 16
PTF12ffs	P200	DBSP	2012 Jul 21
PTF12fhz	Keck II	DEIMOS	2012 Jul 16
PTF12fhz	Keck I	LRIS	2012 Jul 18
PTF12fhz	Keck I	LRIS	2012 Jul 19
PTF12fhz	Keck I	LRIS	2012 Sep 19
PTF12fhz	Keck I	LRIS	2013 Feb 09
PTF12fkp	Keck I	LRIS	2012 Jul 15
PTF12fkp	Keck I	LRIS	2012 Jul 15
PTF12fkp	Keck I	LRIS	2012 Aug 19
PTF12ftc	Keck I	LRIS	2012 Jul 15
PTF12ftc	Keck I	LRIS	2012 Jul 15
PTF12ftc	P200	DBSP	2012 Jul 27
PTF12glz	P200	DBSP	2012 Jul 15
PTF12glz	P200	DBSP	2012 Jul 26
PTF12glz	Keck I	LRIS	2013 Feb 09
PTF12glz	Keck I	LRIS	2013 May 09
PTF12gnt	APO	DIS	2012 Jul 16
PTF12gnt	Keck I	LRIS	2012 Jul 16
PTF12gnt	P200	DBSP	2012 Jul 21
PTF12gnt	P200	DBSP	2012 Jul 26
PTF12gnt	Keck I	LRIS	2012 Aug 18

Keck I LRIS - Keck I 10 m telescope Low Resolution Imaging Spectrometer

Keck II DEIMOS - Keck II 10 m telescope DEep Imaging Multi-Object Spectrograph

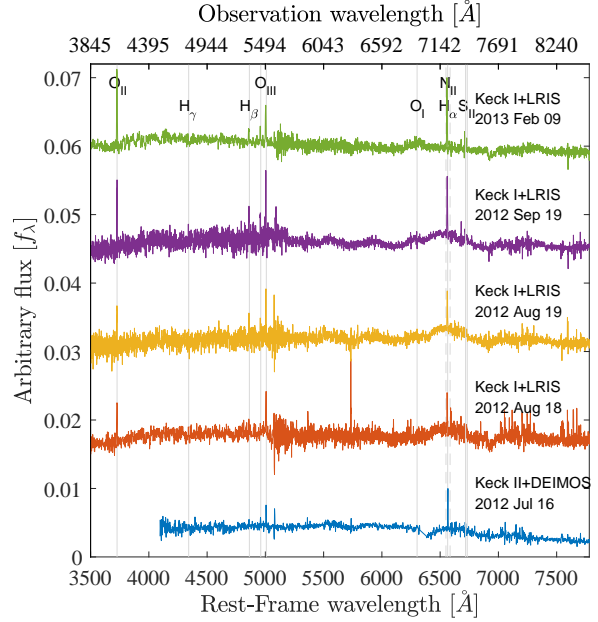
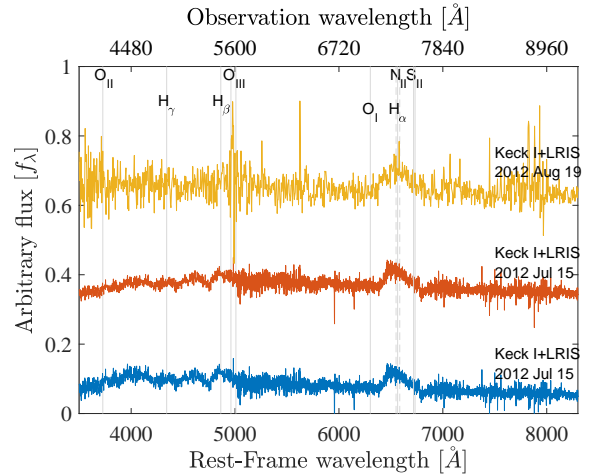
APO DIS - Apache Point Observatory 3.5 m telescope Dual Imaging Spectrograph

P200 DBSP - Palomar 200-inch Hale telescope Double Beam Spectrograph

rial (CSM). Therefore they can be applied only for SNe with no evidence for CSM interaction in their spectra. The free parameters we fit are the progenitor radius (R_*), shock velocity parameter (v_{s*}), ejecta mass (M_{ej}), progenitor envelope structure parameter (f_ρ), reference time (t_{ref}) and the extinction (E_{B-V}). The shock velocity parameter v_{s*} is defined by the Gandel’Man-Frank-Kamenetskii-Sakurai self-similar solutions (Gandel’Man & Frank-Kamenetskii 1956; Sakurai 1960) for shockwave propagation for a thin shell near the edge of the progenitor, $\delta \equiv (R_* - r)/R_* \ll 1$:

$$v_{sh}(\delta) = v_{s*} \delta^{-\beta n}, \quad (1)$$

where r is the shell initial radius, $n = 3/2(3)$ is the polytropic index for convective (radiative) envelopes (Matzner & McKee 1999), $v_{sh}(\delta)$ is the shock velocity of the shell δ and $\beta = 0.191(0.186)$. f_ρ is defined by the

**Figure 2.** Spectra of PTF12fhz (see Table 4). We used H_α , H_β , H_γ , O_I , O_{II} , O_{III} , N_{II} and S_{II} common galaxy lines (plotted) to measure a red shift of 0.0987.**Figure 3.** Spectra of PTF12fkp (see Table 4). We used H_α , H_β , H_γ , O_I , O_{II} , O_{III} , N_{II} and S_{II} common galaxy lines (plotted) to measure a red shift of 0.12. The Keck I LRIS spectrum from Aug 19th was binned to reduce noise.

progenitor density profile near its surface,

$$\rho_0 = f_\rho \bar{\rho}_0 \delta^n, \quad (2)$$

where $\bar{\rho}_0 = 3M_{ej}/(4\pi R_*^3)$. The reference time (t_{ref}) is the model zero time (see discussion in §3.1 below). A problem with the RW11 and SW16 models is that the time range during which they are valid depends on

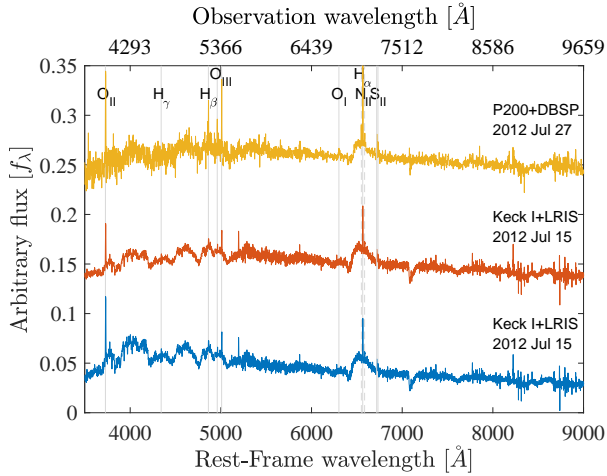


Figure 4. Spectra of PTF12ftc (see Table 4). We used H_α , H_β , H_γ , O_I , O_{II} , O_{III} , N_{II} and S_{II} common galaxy lines (plotted) to measure a red shift of 0.0732.

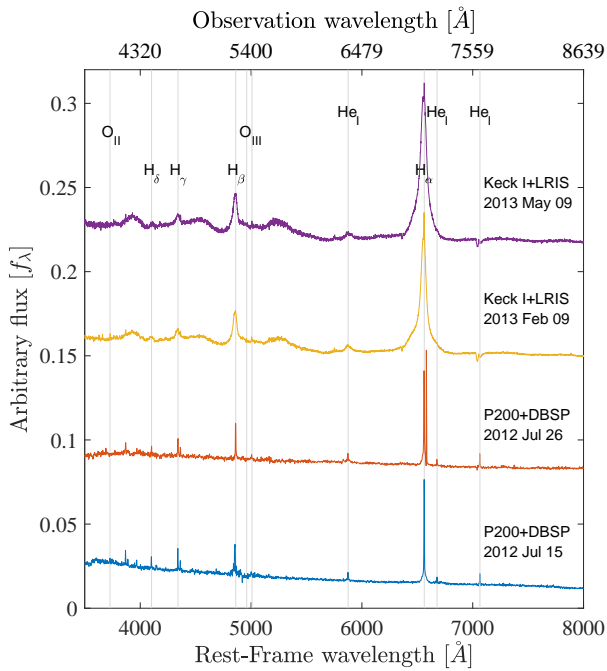


Figure 5. Spectra of PTF12glz (see Table 4). We used H_α , H_β , H_γ , H_δ , He_I , O_{II} , and O_{III} lines (plotted) to measure a red shift of 0.0799.

the physical parameters we are attempting to fit. This means that not all the observations can be used, and that the specific observations that can be used (and hence the number of degrees of freedom) depend on the model parameters. Furthermore, this also means that there are regions in the phase space which we cannot

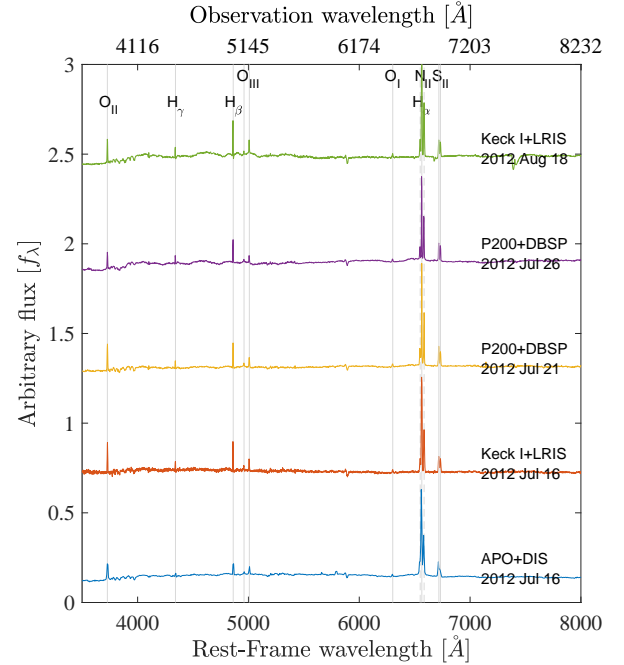


Figure 6. Spectra of PTF12gnt (see Table 4). We used H_α , H_β , H_γ , O_I , O_{II} , O_{III} , N_{II} and S_{II} common galaxy lines (plotted) to measure a red shift of 0.029.

constrain. This problem is partially alleviated with the introduction of the MSW20 model extension, which is valid from the earliest time relevant to our observations, but still affects the model validity for the late data points (See for example the model validity range in Figure 11; each model is plotted only within its validity period). We note that this is an important limitation of the models and this fact is sometime ignored in the literature and may lead to biased results (see the discussion in Rubin & Gal-Yam 2017).

Comparison between RW11 and other shock-cooling models, for example, those of Nakar & Sari (2010) was reported by Sapir & Waxman (2017). In particular, RW11 find that the temperature $T \sim t^{-0.45}$ while Nakar & Sari (2010) consistently find $T \sim t^{-0.4} - t^{-0.6}$ during the relevant phases. Since the temporal dependency of both models is similar, the low cadence of our data does not allow us to distinguish between the two. Here, we use the model of SW17, an extension of RW11 which allows us to use late data points extending beyond the original RW11 validity range (see below), as well as the extension of MSW20, which allows us to utilize the light curve early data points, before RW11 and SW17 become valid.

3.1. Model Description and Limitations

RW11 derive the radius and temperature of the photosphere, in a thin layer near the edge of the progenitor $\delta = 1 - r/R_* \ll 1$, where r is the pre-explosion radius of the shell. Here, we use their main results but we limit the discussion to red supergiants with $n = 3/2$. The photosphere temperature and bolometric luminosity are given by (only $n = 3/2$ values are given, see RW11 and SW17 for $n = 3$ values)

$$\begin{aligned} T_{\text{ph,RW}} &= 1.61 \left(\frac{v_{s*,8.5}^2 t_d^2}{f_\rho M_0 \kappa_{0.34}} \right)^{\epsilon_1} \frac{R_{13}^{1/4}}{\kappa_{0.34}^{1/4}} t_d^{-1/2} \text{ eV}, \\ L_{\text{RW}} &= 2.0 \times 10^{42} \left(\frac{v_{s*,8.5}^2 t_d^2}{f_\rho M_0 \kappa_{0.34}} \right)^{-\epsilon_2} \frac{v_{s*,8.5}^2 R_{13}}{\kappa_{0.34}} \text{ erg s}^{-1}, \end{aligned} \quad (3)$$

where $R_* = 10^{13} R_{13} \text{ cm}$, $M_{\text{ej}} = 10^0 M_0 M_\odot$, $v_{s*} = 10^{8.5} v_{s*,8.5} \text{ cm s}^{-1}$, $\kappa = 0.34 \kappa_{0.34} \text{ cm}^2 \text{ g}^{-1}$, t_d is the time elapsed since t_{ref} in days and the power-laws are $\epsilon_1 = 0.027$ and $\epsilon_2 = 0.086$. We have used a constant opacity of $\kappa_{0.34} = 1$ for all the calculations in this paper.

Some papers confuse the model parameter t_{ref} , with the SN explosion time t_{exp} or with the shock break out time t_{BO} . In general, $t_{\text{ref}} \neq t_{\text{BO}} \neq t_{\text{exp}}$, since RW11 is focused on late times and therefore ignores the shells initial radius, and their acceleration to their final velocity

$$r(\delta_m, t) = v_f(\delta_m) t, \quad (4)$$

where δ_m is a notation for the layer for which a fraction δ_m of the progenitor mass lies ahead of. These approximations are justified when dealing with the shock cooling phase of the explosion, after a significant expansion of the ejecta. However, if we try to put some physical meaning to t_{ref} , the time $t_d = 0$, Eq. 4 will give us $r(\delta_m, 0) = 0$ which is clearly wrong. Since each layer starts at a finite radius $r_0(\delta_m)$, the time t_{ref} (i.e., $t_d = 0$), is always earlier than t_{BO} , the time the shock breaks out from the progenitor surface. We can estimate the time difference between t_{BO} and t_{ref} by calculating the time it takes a layer to artificially expand from 0 to r_0 at a velocity v_f , the final velocity of the shell after its acceleration phase is completed. This time is estimated to be of order of 1 day, for large stars $R_* \approx 1000 R_\odot$. Therefore we can conclude that t_{ref} is about 1 day before the shock breakout.

Both the RW11 and SW17 models become valid only when the ejecta shells have expanded significantly, reaching their terminal velocity, and when the photosphere penetrates deeper than the layer at which the initial breakout took place. These two conditions are

met at

$$t > t_{\text{min}} = 0.2 \frac{R_{13}}{v_{s*,8.5}} \max \left[0.5, \frac{R_{13}^{0.4}}{(f_\rho \kappa_{0.34} M_0)^{0.2} v_{s*,8.5}^{0.7}} \right] \text{ days.} \quad (5)$$

The models assume a highly ionized envelope (RW11 deals with H, He and C/O envelopes while SW17 use a solar composition for the envelope), where the opacity is dominated by Thomson scattering, and a constant opacity approximation can be used. This approximation does not hold when the temperature drops below $\approx 0.7 \text{ eV}$ and a significant Hydrogen recombination takes place, which reduces the opacity sharply. The time at which the temperature is above 0.7 eV is given by

$$t \lesssim t_{\text{opac}} = 6.47 \left(\frac{v_{s*,8.5}^2}{f_\rho M_0 \kappa_{0.34}} \right)^{0.061} \left(\frac{R_{13}}{\kappa_{0.34}} \right)^{0.56} \text{ days.} \quad (6)$$

Even when the constant opacity approximation holds, RW11 breaks when the photosphere penetrates deeper into the progenitor shells and violates the model small δ approximation. The time at which the photosphere penetrates to a depth of $\delta \lesssim 0.1$ is given by

$$t < t_\delta = 3 f_\rho^{-0.1} \frac{\sqrt{\kappa_{0.34} M_0}}{v_{s*,8.5}} \text{ days.} \quad (7)$$

RW11 results are independent of the progenitor density profile as the outer shells of the envelope, for which $\delta \ll 1$, are universal for all progenitors with the same polytropic index n . SW17 extends RW11 for finite δ , but introduces a dependency on the progenitor's density profile. SW17 is valid up to the point the envelope becomes almost transparent to radiation, t_{tr}/a , where t_{tr} is the time the envelope is expected to become transparent and given by

$$t_{\text{tr}} \cong 19.5 \left(\frac{\kappa_{0.34} M_{\text{env},0}}{v_{s*,8.5}} \right)^{1/2} \text{ days,} \quad (8)$$

a is an order of unity parameter with the value 1.67 for $n = 3/2$ and $M_{\text{env}} = 10^0 M_{\text{env},0} M_\odot$ is the progenitor envelope mass. SW17 suppresses RW11 bolometric luminosity according to ($n = 3/2$ values were used)

$$L/L_{\text{RW}} = 0.94 \exp \left[- \left(\frac{at}{t_{\text{tr}}} \right)^{0.8} \right]. \quad (9)$$

The SW17 validity extension is dependent on the envelope mass, M_{env} , while the original RW11 part of the model depends on the ejecta mass M_{ej} . These two masses are related by $M_{\text{ej}} = M_{\text{env}} + M_c$, where M_c is the core mass (this relation is described in SW17 §2.2 and

reviewed in [Arcavi et al. 2017](#)). The relation between M_{env} and M_c determines the value of f_ρ :

$$f_\rho \approx \sqrt{M_{\text{env}}/M_c}. \quad (10)$$

In addition to the validity extension, SW17 also recommend to use the ratio $f_T = T_{\text{col}}/T_{\text{ph}}=1.1$ rather than 1.2 suggested by RW11 due to the use of solar composition for the envelope instead of pure Hydrogen one.

3.2. Morag-Sapir-Waxman model extension

Morag et al. (2020, in preparation) extends the lower validity limit of the RW11 and SW17 models. It utilizes the asymptotic solution of the [Sapir et al. \(2011\)](#); [Katz et al. \(2012\)](#); [Sapir et al. \(2013](#), hereafter SKW13) shock break out model as the solution for times earlier than t_{min} (Eq. 5) and connect it to the SW17 shock cooling solution. The asymptotic solution of the break out model, translated to SW17 variables is given by

$$L_{\text{SKW}} = 2.97 \times 10^{42} \frac{R_{13}^{2.46} v_{s*,8.5}^{0.60}}{(f_\rho M_0)^{0.06} \kappa_{0.34}^{1.06}} t_{\text{hr}}^{-4/3} \text{ erg s}^{-1}, \quad (11)$$

where $t = 1t_{\text{hr}}$, and

$$T_{\text{SKW}} = 6.94 \frac{R_{13}^{0.12} v_{s*,8.5}^{0.15}}{(f_\rho M_0)^{0.02} \kappa_{0.34}^{0.27}} t_{\text{hr}}^{-1/3} \text{ eV}. \quad (12)$$

The asymptotic luminosity of the break out solution decays $\propto t^{-4/3}$ while the SW17 luminosity is almost constant $\propto t^{-0.086}$. At t_{min} (Eq. 5), when SW17 becomes valid, the breakout luminosity almost completely vanishes. Therefore the we can use the sum

$$L_{\text{MSW}} = L_{\text{SKW}} + L_{\text{SW}}, \quad (13)$$

to tie the two solutions. The asymptotic break out temperature decays slower ($\propto t^{-1/3}$) than the SW17 solution ($\propto t^{-1/2}$). Therefore, the transition between the temperatures of the planar and spherical solutions is given by

$$T_{\text{MSW}} = f_T \min[T_{\text{SKW}}, T_{\text{SW}}]. \quad (14)$$

The full model which includes the SKW13 planar break out asymptotic solution and the SW17 spherical shock cooling solution was tested against numerical hydrodynamic simulations and was found to describe well (up to an error of +10%/-30%) the simulation results, starting at

$$t_{\text{min,MSW}} = 3R_*/c = 17R_{13} \text{ min}. \quad (15)$$

At this time, the asymptotic break out solution is valid, and the spectrum is described well by a modified black body (i.e. with a shape of a black body spectrum, but with a luminosity different than $4\pi R^2 \sigma_B T^4$), with

$f_T = 1.1$, and where σ_B is the Stefan-Boltzmann constant. Although the SKW13 reference time is t_{BO} , at t_{MSW} the photosphere is expanded enough and the difference between time elapsed since t_{BO} and the SW17 t_{ref} does not introduce a significant contribution to the bolometric luminosity or to the photosphere temperature, allowing both parts of the model to refer to t_{ref} .

3.3. SOPRANOS Fitting Procedure

The challenge we face is to compare different models, where each model is valid for a different period of time and therefore for different subset of the data. The traditional fitting procedures compare all the models to a fixed subset of data points (e.g. [Valenti et al. 2014](#); [Bose et al. 2015](#); [Rubin et al. 2016](#); [Hosseinzadeh et al. 2018](#)). The selection of a fixed subset of the data may limit the explored region of the parameters space and may prefer models whose validity region coincidentally matches the selected data subset over models with partial overlap. At an extreme case the method best fit may be invalidated by valid data points external to the fixed subset.

The SOPRANOS (ShOck cooling modeling with saPiR & wAxman model by gANot & Soumagnac) fitting procedure utilizes *all* the valid data points corresponding to each model and *only* those data points, by calculating the models likelihood. SOPRANOS has two implementations. SOPRANOS-grid, described in this paper and written in MATLAB, which samples the parameter space by calculating the likelihood of a discrete grid of models, and SOPRANOS-nested, described on [Soumagnac et al. \(2020\)](#) and written in python, which uses the nested sampling algorithm ([Skilling 2004, 2006](#); [Higson et al. 2019](#); [Speagle 2020](#)) to dynamically sample the model parameter space.

Before fitting the model parameters with the SOPRANOS algorithm we measure the SN redshifts from their spectra by identifying host galaxy lines. We also measure the *NUV* background for each SN *NUV* light curve from data points before and after the SN, in order to remove the host galaxy contribution from the SN measurements (both values appear in Table 1, the measurement of the *NUV* background is described in §3.4). The redshift and *NUV* background values are fixed and common for all the models of a SN and are not free model parameters we estimate.

With the redshift and background levels in hand, we calculate the expected flux in the two bands (*GALEXNUV* and PTF *R*-band), for each model defined by a combination of the physical parameters using the MATLAB Astronomy and Astrophysics Toolbox

(MAAT; Ofek 2014)⁵ package. The bolometric luminosity, color temperature and the model validity period are calculated using the `sn_cooling_msw` function. The spectrum of each band at the observer frame was calculated by

$$f_\lambda = \frac{L_{\text{MSW}}}{4\pi D^2} \times \frac{(1+z)^4 B_\lambda [T_{\text{col}}/(1+z)]}{\sigma T_{\text{col}}^4}, \quad (16)$$

where L_{MSW} is the photosphere bolometric luminosity, $T_{\text{col}} = T_{\text{MSW}}(t_d, f_T = 1.1)$ is the color temperature (see Eq. 13, 14), D is the luminosity distance and

$$B_\lambda = \frac{2\pi hc^2}{\lambda^5} \frac{1}{\exp(\frac{hc}{\lambda k_B T}) - 1}, \quad (17)$$

is the Planck equation. $B_{\lambda,z} = (1+z)^4 B_\lambda [T/(1+z)]$ is the redshifted Planck equation. The bolometric flux $\int_0^\infty B_{\lambda,z} d\lambda = \int_0^\infty B_\lambda d\lambda = \sigma_B T^4$ is independent of redshift and therefore the temperature in the right hand side of the denominator of Eq. 16 uses the color temperature at the SN frame. With the predicted spectrum, and the filter transmission curves, we use the `synphot` function for photon counting devices to calculate the exact flux expected for each of the bands. Note that `synphot` applies an extinction correction for each bin of the input spectrum before integrating the spectrum to find the filter magnitude, as required. This method returns a different result compared with first calculating the filter magnitude and then applying the extinction using the filter pivot wavelength. This fact is important when dealing with the *NUV* band, where the extinction curve has a significant slope.

To calculate $\mathcal{P}(\mathcal{M}_j|D)$, the posterior probability of the model \mathcal{M}_j , defined by the set of physical parameters $\{R_*^j, v_{s*}^j, M_{\text{ej}}^j, f_\rho^j, t_{\text{ref}}^j, E_{\text{B-V}}^j\}$, where j is the model index, given the observation data set $D = \{t_i, f_i, \sigma_i\}$, we first find the subset of data points which are within the \mathcal{M}_j valid period:

$$\mathcal{V}_j = \left\{ \{t_i, f_i, \sigma_i\} \mid t_{\text{MSW},z}^j \leq (t_i - t_{\text{ref}}^j) \leq \min(t_{\text{opac},z}^j, t_{\text{tr},z}^j/a) \right\}, \quad (18)$$

where the index i stands for the i^{th} data point in D , and where $t_{\text{MSW},z}^j = (1+z)t_{\text{min,MSW}}^j$, $t_{\text{opac},z}^j = (1+z)t_{\text{opac}}^j$ and $t_{\text{tr},z}^j/a = (1+z)t_{\text{tr}}^j/a$ are the redshifted $t_{\text{min,MSW}}$, t_{opac} and t_{tr} for the model \mathcal{M}_j (see Equations 6, 8 and 15 and text above Equation 8). The model validity times are redshifted since the measurements were taken at the observer frame and not in the SN rest frame where those times are defined.

Assuming Gaussian statistics and that the data points are independent, we calculate the χ^2 sum over the valid data points for the model \mathcal{M}_j

$$\chi_j^2 = \sum_{i \in \mathcal{V}_j} \frac{\{f_i - f^j[(t_i - t_{\text{ref}}^j)/(1+z)]\}^2}{\sigma_i^2}, \quad (19)$$

where $f^j(t_d)$ is the predicted flux at time t_d by the model \mathcal{M}_j , the time difference is blueshifted since the model is defined in the SN rest frame. The number of degrees of freedom for the model \mathcal{M}_j is the number of valid data points ($N_j = |\mathcal{V}_j|$) less the number of free parameters we estimate, which is six for our case. We end this step by calculating the likelihood to measure those data points given the model \mathcal{M}_j :

$$\mathcal{L}(D|\mathcal{M}_j) = \mathcal{P}_{\chi^2}(\chi_j^2, N_j - 6), \quad (20)$$

where $\mathcal{P}_{\chi^2}(\chi^2, N)$ is the χ^2 probability distribution function with N degrees of freedom. The comparable quantity between models is their posterior probability, $\mathcal{P}(\mathcal{M}|D)$. To calculate it we utilize Bayes' theorem:

$$\mathcal{P}(\mathcal{M}|D) = \frac{\mathcal{L}(D|\mathcal{M})\mathcal{P}(\mathcal{M})}{\mathcal{P}(D)}, \quad (21)$$

where \mathcal{M} is the model, D is the data, $\mathcal{P}(\mathcal{M})$ is the prior and $\mathcal{P}(D)$ is the probability to measure this data which is constant independent of the model. Now we can compare the posterior probabilities of different models. Since we are using a conservative flat prior (see §3.5), and since $\mathcal{P}(D)$ is a constant independent of model, the posterior probability of a model is proportional to the likelihood to measure the data given the same model. We use the posterior probability to compare between models, and therefore we can ignore the constant proportion factor, and to compare the likelihood to measure our data given the different models as a discrimination measure between the different models.

At this point we have a grid of models, and for each model we have the likelihood to measure the data set $D = \{t_i, f_i, \sigma_i\}$ given this model, which is proportional to its posterior probability. Assuming the grid is dense enough, the shape of the discrete likelihood function describes well the behaviour of the continuous one. However, the values of the grid maxima are not the most likely models, since the grid models are limited to the arbitrary choice of the grid parameters values. To get the most likely models we numerically find the maxima of the continuous likelihood function, using the discrete grid maxima as initial conditions.

Recognizing R_* and v_{s*} are the dominant parameters of the models (see Eq. 3, 11 and 12), we start the optimization by marginalizing over M_{ej} , f_ρ , t_{ref} , and $E_{\text{B-V}}$

⁵ <https://webhome.weizmann.ac.il/home/eofek/matlab/>

and look for the local maxima of the two dimensional likelihood grid spanned by these two parameters. We ignore local maxima smaller than 1% of the global grid maximum to avoid insignificant peaks resulting from numerical noise. For each one of the local maxima we repeat the following three stage optimization: At the first stage we allow only R_* and v_{s*} to vary, while for the rest of the parameters we use their grid values, and marginalizing over them to calculate the the likelihood. At the second stage we freeze R_* and v_{s*} values to the result of the first stage and allow M_{ej} , f_ρ , t_{ref} , and E_{B-V} to vary (their initial values are the maximum value of the four dimensional grid calculated in the first stage for the purpose of marginalization of those parameter). The last stage allows all the six parameters to vary, where the initial values are the result of the second stage. The numerical optimization uses MATLAB’s `fminsearch` function with $1 - \mathcal{L}(D|\mathcal{M})$ as the objective function. We report the optimization results for all the local maxima in a table for each SN.

First results of the SOPRANOS algorithm were already reported in Soumagnac et al. (2020) which used SOPRANOS-nested. Here we use SOPRANOS-grid. The two implementation are complimentary to each other. The grid implementation is useful to map the proper prior ranges for a SN (where the marginal likelihood distribution for each parameter converges asymptotically to 0, see §3.5) and is independent of a specific sampling algorithm while the nested implementation has a higher resolution for the physical parameters and does not require a numerical optimization. Another advantage of these two implementation is the ability to test and verify them one against the other. The SOPRANOS-grid implementation was added to the MAAT toolbox (Ofek 2014).

3.4. UV Background

The SOPRANOS algorithm assumes the data points are background subtracted (including any host contribution) and all the measured flux comes from the SN. The GALEX data analysis is not based on image subtraction and therefore may include some residual light from the SN host galaxy, and this contribution needs to be removed.

The data points before the SN rise are natural candidates to measure the *NUV* background level. However, since some SNe were detected at the beginning of the experiment, we have only a small number of data points before the SN. The shock cooling models predict that the *NUV* signal of the SN will decay and disappear as the ejecta cools down. We also see this behaviour in the observations themselves, which means that late *NUV*

data points after the *NUV* transient may also be used for the measurement of the *NUV* background.

The first step in measuring the background level is to identify the SN transient in the *NUV*. We compared all the data points to an initial reference background level from previous GALEX images, where available, or to the lower 25th percentile of data points, where previous archival GALEX images were not available. We identify the SN transient beginning by a data point whose flux is larger than the reference background by more than 3σ and its end by the last data point with flux larger than the initial background by more than 1σ . The different criteria for the beginning and the ending of the transient are a result of the model prediction of the photosphere cooling and therefore lower *NUV* signal towards the end of the transient. If we were using a symmetrical criterion of 3σ , data points which contain contribution from the SN would have been considered as not part of the transient, leading to an over estimation of the background level. We calculate the background value by comparing data points before and after the transient to a constant flux model, and minimize χ^2 with respect to those points.

3.5. Priors

As described on section 3.3, we are fitting six parameters for the model R_* , v_{s*} , M_{ej} , f_ρ , t_{ref} and E_{B-V} and using Bayes theorem. This requires some priors, which have to be selected carefully in order not to bias the results. Davies et al. (2018) explored the population of Red Super Giants in the Small and Large Maglanic Clouds and derived their radius out of the measured luminosity and temperatures (See Figure 10 on Soumagnac et al. 2020). Most of the RSGs have radii smaller than 1100 solar radii, and only a few have radii in the range of 1100–1400 solar radii. We have chosen the range of 200–2000 solar radii as a flat conservative prior for the progenitor radius.

The v_{s*} prior was selected iteratively, starting from a range of $1.6 \times 10^8 - 9.5 \times 10^8$ cm s⁻¹ ($v_{s*,8.5}=0.5-3$) and adjusting it according to the marginalized distribution we receive until the tails of the marginalized distribution asymptotically reach 0. Typically this process converged to $v_{s*,8.5}$ values in the range of 0.4 to 5. M_{ej} was chosen in the range of 2–20 solar masses. f_ρ was selected in the range of $\sqrt{1/3}$ and $\sqrt{10}$, reflecting the range of M_c/M_{env} simulation cases tested by SW17 to validate their model (see Eq. 10 for the relation between f_ρ and M_c/M_{env}). The t_{ref} prior was chosen from the last non-detection to the first detection in one of the two bands. E_{B-V} lower limit is constrained by the local galaxy extinction map of Schlegel et al. (1998) and the upper limit was selected

Table 5. GALEX/PTF SOPRANOS maximum likelihood models

PTF name	R_*	$v_{s*,8.5}$	M_{ej}	f_ρ	t_{ref}	E_{B-V}	χ^2/dof
PTF12gnt ^a	418_{-2}^{+403}	$1.43_{-0.65}^{+0.00}$	$2.2_{-0.2}^{+5.2}$	$0.577_{-0.000}^{+0.575}$	$56111.20_{-0.44}^{+0.00}$	$0.052_{-0.006}^{+0.027}$	$33.37/20^{\text{b}}$
PTF12gnt ^a	636_{-216}^{+185}	$0.86_{-0.22}^{+0.17}$	$3.0_{-1.0}^{+4.5}$	$2.744_{-2.079}^{+0.027}$	$56111.00_{-0.25}^{+0.19}$	$0.048_{-0.001}^{+0.031}$	$65.25/37^{\text{b}}$
PTF12ffs ^c	788_{-244}^{+248}	$1.03_{-0.17}^{+0.21}$	$5.0_{-3.0}^{+4.2}$	$1.794_{-1.129}^{+0.192}$	$56077.50_{-0.47}^{+0.54}$	$0.040_{-0.015}^{+0.028}$	17.00/19
PTF12fhz	249_{-149}^{+869}	$3.36_{-1.10}^{+0.00}$	$2.5_{-2.0}^{+10.6}$	$0.684_{-0.507}^{+0.000}$	$56086.06_{-0.33}^{+0.42}$	$0.089_{-0.002}^{+1.22}$	0.61/2
PTF12fkp	1262_{-511}^{+441}	$1.85_{-0.28}^{+0.27}$	$2.1_{-0.1}^{+3.8}$	$1.824_{-1.158}^{+0.101}$	$56084.20_{-0.90}^{+0.14}$	$0.026_{-0.000}^{+0.061}$	12.90/14
PTF12ftc	895_{-621}^{+487}	$1.09_{-0.27}^{+0.43}$	$2.0_{-0.0}^{+9.0}$	$2.395_{-1.628}^{+0.293}$	$56089.49_{-1.15}^{+0.50}$	$0.038_{-0.001}^{+0.272}$	13.00/15
PTF12glz ^d							

^a PTF12gnt likelihood map has multiple peaks. We report here two characterizing solutions.

^b PTF12gnt data include three suspicious points which do not fit any model, and contribute about 10 units to χ^2 .

^c PTF12ffs solutions have a degeneracy in f_ρ and M_{ej} values, their multiplication is the measured quantity (see text).

^d PTF12glz is a type IIn SN which includes interaction with the CSM which is not modeled by MSW20. It is analyzed by Soumagnac et al. (2019).

iteratively according to the result marginal distribution, until its likelihood asymptotically converged to 0.

For PTF12fhz which has a double-peaked light curve, sometimes observed in other Type IIb SN, we chose some different priors. SW17 have shown their model may explain the first peak for $R_* \approx 500R_\odot$ and $M_{\text{env}} < 1M_\odot$ (See their §5). We changed our priors for this SN to improve the resolution of the parameters in the regime described by SW17. The progenitor radius prior lower end was extended to $100R_\odot$, the ejecta mass lower limit was extended to $0.5M_\odot$ and its grid values was spanned logarithmically to improve the resolution for low masses. f_ρ lower end was extended to 0.1 to allow small values of M_{env} . Note that SW17 was not tested against simulations with f_ρ smaller than $\sqrt{1/3}$ and therefore the results for these low values should be taken with caution (SW17 used $f_\rho = 0.3$ to describe this type of SNe).

4. RESULTS

Table 5 summarizes the maximum likelihood model for each one of the GALEX/PTF SNe. For each SN we also present the spectra used to measure the redshift, the SN data points together with its maximum likelihood model-predicted light curves, the best-fit residuals for the maximum likelihood models, the marginalized $R_*-v_{s*,8.5}$ likelihood map, the marginalized distributions for M_{ej} , f_ρ , t_{ref} and E_{B-V} and list all the models the SOPRANOS algorithm converged to.

4.1. PTF12ffs

PTF12ffs data points together with its most likely models appear in Figure 7, while the most likely best-fit residuals are presented in Figure 8. The marginalized R_*-v_{s*} likelihood map and the marginalized likelihood for each parameter are plotted in Fig. 9 and the marginalized likelihood distributions for M_{ej} , f_ρ , t_{ref} and

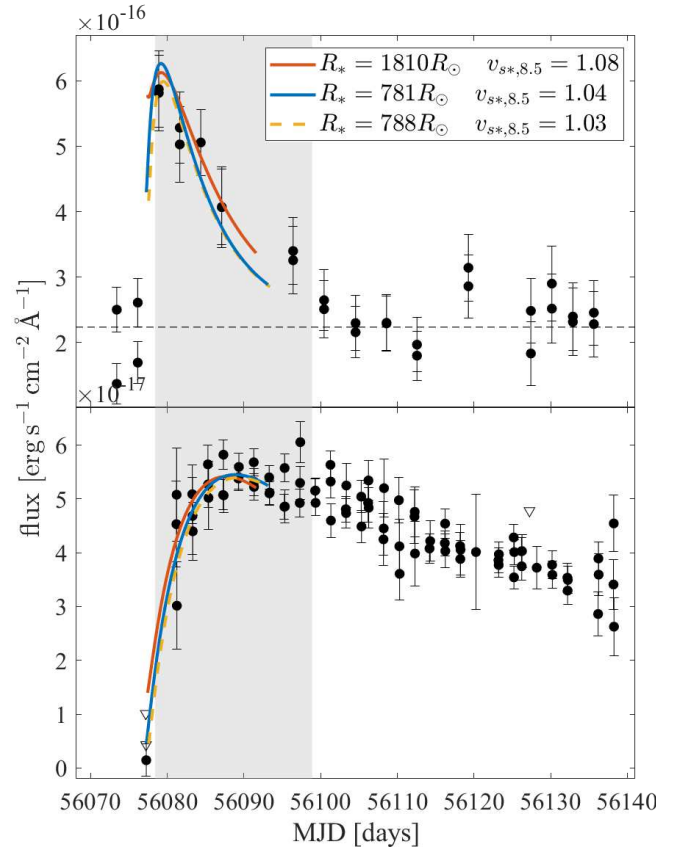


Figure 7. PTF12ffs data points and best fitting models. The upper panel describes the *NUV* band data and the lower one is for the *R* band. The dashed horizontal line in the upper panel represents the measured *NUV* background. The triangles in the bottom panel stand for 3σ limits. The colored lines show the different solutions. The R_* and v_{s*} values for these solutions are listed in the legend while the other parameters are in Tables 6 and 7. The grayed background area marks the *NUV* transient. *NUV* data points external to this area were used to calculate the *NUV* background.

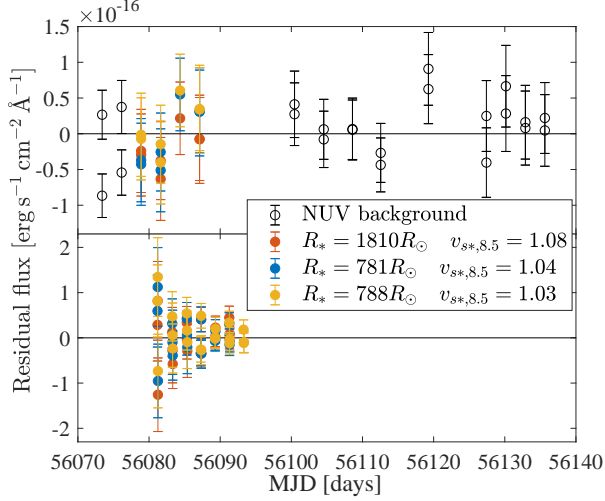


Figure 8. PTF12ffs best-fit residuals for the models plotted in Fig. 7. The upper panel shows the *NUV* band residuals and the bottom panel the *R* band. The color code is the same as in Fig. 7. The empty black circles are the residuals of the *NUV* background estimation.

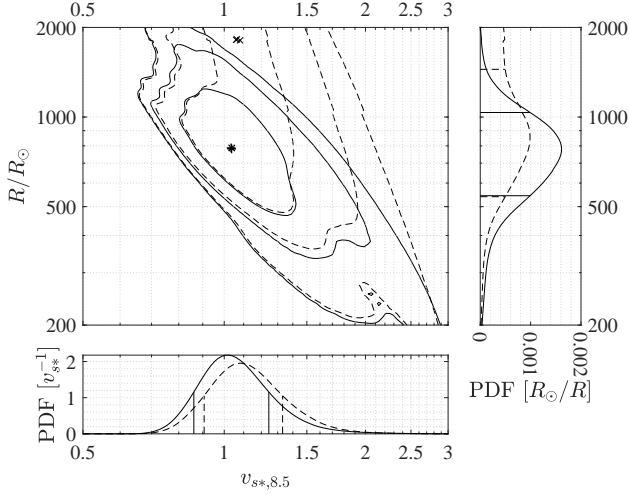


Figure 9. PTF12ffs R_* - v_{s*} likelihood map. The solid contour lines represents 1σ , 2σ and 3σ of the cumulative likelihood with an extinction prior of $0.025 \leq E_{B-V} \leq 0.09$ Mag, and the dashed contour represents the cumulative likelihood with extinction prior of $0.025 \leq E_{B-V} \leq 0.26$ Mag. The plus markers indicate maximal likelihood models for the first extinction prior while the cross symbols are for the maximal likelihood models for the second extinction prior. The bottom and right panels show the marginal distribution for v_{s*} and R_* where the solid line plots the marginal distribution for the first prior and the dashed ones for the second. The vertical (horizontal) lines stand for the marginal distributions 1σ .

E_{B-V} are shown in Fig. 10. The local maxima of the likelihood function are listed in Table 6.

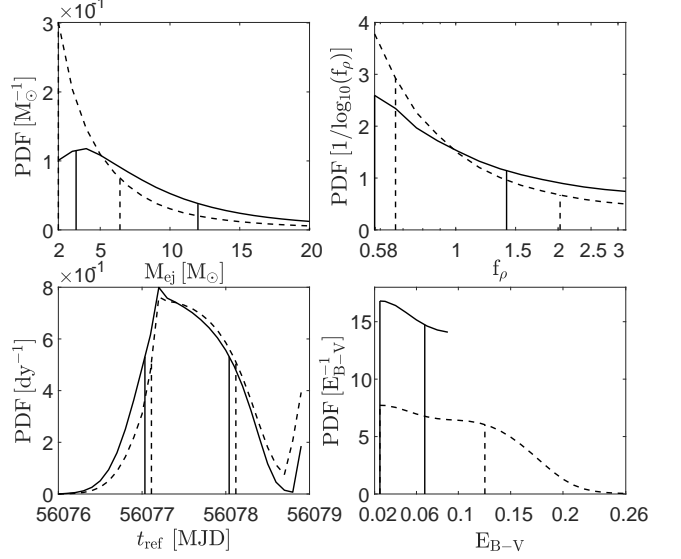


Figure 10. PTF12ffs Marginal distributions for M_{ej} , f_ρ , t_{ref} and E_{B-V} . Solid lines represent the marginal distributions for an extinction prior of up to 0.09 Mag while the dashed ones plot the distributions for a prior of up to 0.26 Mag.

Table 6. PTF12ffs Likelihood local maxima $0.025 \leq E_{B-V} \leq 0.26$ Mag

Parameter	Peak #1	Peak #2	Peak #3
R_* [R_\odot]	1810^{+0}_{-1042}	1824^{+0}_{-1049}	786^{+661}_{-246}
$v_{s*,8.5}$	$1.08^{+0.25}_{-0.17}$	$1.06^{+0.27}_{-0.16}$	$1.04^{+0.29}_{-0.13}$
M_{ej} [M_\odot]	$2.0^{+4.4}_{-0.0}$	$2.0^{+4.4}_{-0.0}$	$12.0^{+1.3}_{-9.0}$
t_{ref} [MJD]	$56077.27^{+0.85}_{-0.16}$	$56077.10^{+1.01}_{-0.00}$	$56077.30^{+0.82}_{-0.19}$
f_ρ	$1.536^{+0.491}_{-0.871}$	$1.556^{+0.471}_{-0.890}$	$0.665^{+0.523}_{-0.088}$
E_{B-V}	$0.133^{+0.000}_{-0.102}$	$0.131^{+0.000}_{-0.101}$	$0.030^{+0.095}_{-0.005}$
χ^2/dof	14.00/ 16	14.23/ 16	17.00/ 19
Parameter	Peak #4	Peak #5	
R_* [R_\odot]	789^{+658}_{-249}	1817^{+0}_{-1045}	
$v_{s*,8.5}$	$1.04^{+0.30}_{-0.13}$	$1.06^{+0.27}_{-0.15}$	
M_{ej} [M_\odot]	$5.0^{+1.4}_{-3.0}$	$7.0^{+6.4}_{-4.0}$	
t_{ref} [MJD]	$56077.60^{+0.52}_{-0.49}$	$56077.40^{+0.72}_{-0.29}$	
f_ρ	$1.794^{+0.233}_{-1.129}$	$0.577^{+0.611}_{-0.000}$	
E_{B-V}	$0.040^{+0.085}_{-0.015}$	$0.150^{+0.000}_{-0.107}$	
χ^2/dof	17.00/ 19	17.00/ 19	

Examining Figure 9 we notice the likelihood distribution (dashed contour) includes two peaks (cross markers), one at $R_* \cong 800R_\odot$ and the second at $R_* \cong 1800R_\odot$. The radius marginal likelihood distribution has a non-negligible values for radius values greater than $2000R_*$, values which are not physical for the expected RSG progenitors. We try to separate between the two peaks in order to focus on the more physical solutions. The higher radius solutions are associated with

Table 7. PTF12ffs Likelihood local maxima
 $0.025 \leq E_{B-V} \leq 0.09$ Mag

Parameter	Peak #1	Peak #2
R_* [R_\odot]	781^{+254}_{-237}	788^{+248}_{-244}
$v_{s*,8.5}$	$1.04^{+0.21}_{-0.18}$	$1.03^{+0.21}_{-0.17}$
M_{ej} [M_\odot]	$12.0^{+0.0}_{-8.7}$	$5.0^{+4.2}_{-3.0}$
t_{ref} [MJD]	$56077.20^{+0.84}_{-0.17}$	$56077.50^{+0.54}_{-0.47}$
f_ρ	$0.665^{+0.746}_{-0.088}$	$1.794^{+0.192}_{-1.129}$
E_{B-V}	$0.030^{+0.038}_{-0.005}$	$0.040^{+0.028}_{-0.015}$
χ^2/dof	17.00/ 19	17.00/ 19
	Peak #3	Peak #4
R_* [R_\odot]	782^{+253}_{-238}	786^{+249}_{-242}
$v_{s*,8.5}$	$1.04^{+0.21}_{-0.18}$	$1.03^{+0.21}_{-0.17}$
M_{ej} [M_\odot]	$5.0^{+4.2}_{-3.0}$	$12.0^{+0.0}_{-8.7}$
t_{ref} [MJD]	$56077.50^{+0.54}_{-0.47}$	$56077.20^{+0.84}_{-0.17}$
f_ρ	$1.794^{+0.192}_{-1.129}$	$0.665^{+0.746}_{-0.088}$
E_{B-V}	$0.040^{+0.028}_{-0.015}$	$0.030^{+0.038}_{-0.005}$
χ^2/dof	17.00/ 19	17.00/ 19

higher extinction values of $E_{B-V} \gtrsim 0.13$ Mag while the lower radius solutions have lower extinction values of $E_{B-V} \lesssim 0.04$ Mag (Table 6). This degeneracy is a result of the relation $L \propto R_* v_{s*}^2$ (Eq. 3) which causes the higher radius solution to be more luminous. The extinction marginal distribution which appears in Fig. 10 (dashed line) has two local maxima. It includes a main peak at $E_{B-V} \approx 0.025$ Mag and a secondary peak at $E_{B-V} \approx 0.13$ Mag. We chose the point of $E_{B-V} = 0.09$ Mag, where the extinction marginal likelihood distributions becomes flat, as the point which separates between the two peaks and repeated the analysis with narrower extinction prior which includes only values of $0.025 \leq E_{B-V} \leq 0.09$ Mag. The results of the second analysis are plotted with solid lines on Figs. 9 and 10, and its maximal likelihood solutions are marked by plus symbols in Figure 9 and are listed in Table 7. Narrowing the extinction prior made the higher radius peak disappear and all the results models converged to a progenitor radius of $R_* \simeq 790R_\odot$. The most likely models in Table 7 share similar values for all their parameters except for f_ρ and M_{ej} which have a large scatter compared to the other parameters, and are separated into two subgroups: $f_\rho = 0.665$, $M_{\text{ej}} = 12M_\odot$ and $f_\rho = 1.794$, $M_{\text{ej}} = 5M_\odot$. While the two last parameter values have a large scatter, their multiplication, $8M_\odot$ and $9M_\odot$ respectively, has a small scatter, which is comparable to the one of the other parameters. Most of the model equations (3, 5, 6) depend on the multiplication of the two. This degeneracy is removed only at late times by equations 8 and 9, in the case the photosphere becomes transparent before the recombination takes place. For our models

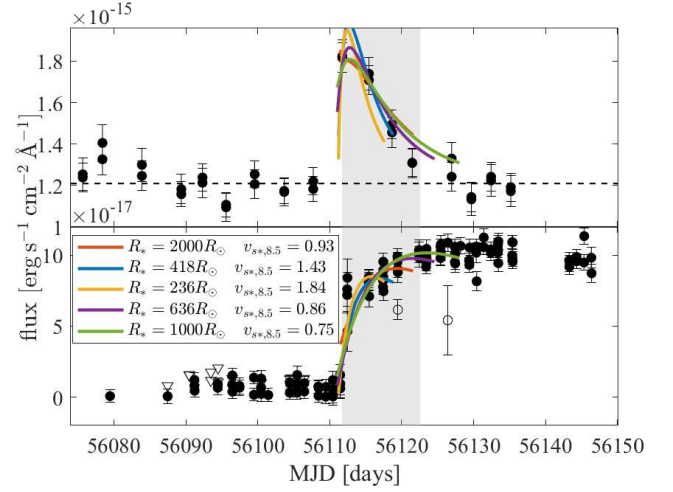


Figure 11. PTF12gnt data points and the best-fitting models. The upper panel describes the *NUV* band data and the lower one is for the *R* band. The dashed horizontal line in the top panel represents the measured *NUV* background. The triangles in the bottom panel stand for 3σ limits and the empty circle error bars are outliers that were removed from the fit. The colored lines show the different solutions. The R_* and v_{s*} values of these solutions are listed in the legend while the other parameters are in Tables 8 and 9. The gray background area marks the *NUV* transient. Data points external to this area were used to calculate the *NUV* background.

$t_{\text{opac}} \approx 15$ days and $t_{\text{tr}} \approx 37$ days so recombination occurs before the photosphere becomes transparent, and the effects which depend on M_{env} become significant. Therefore we cannot solve the degeneracy between f_ρ and M_{ej} for this SN.

4.2. PTF12gnt

PTF12gnt data points together with its most likely models appear in Figure 11. The residuals of the most likely best-fit are presented in Figure 12. The marginalized R_* - v_{s*} likelihood map and the marginalized likelihood for each parameter are plotted in Figure 13 and the marginalized likelihood distributions for M_{ej} , f_ρ , t_{ref} and E_{B-V} are shown in Figure 14. The local maxima of the likelihood function are listed in Table 8 and marked on Figure 12 by cross symbols. As for PTF12ffs, looking at the likelihood distribution map in Fig. 13 (dashed black contours), we can distinguish between solutions with progenitor radius greater and smaller than $1000R_\odot$ by splitting the extinction prior to values smaller or greater than $E_{B-V} = 0.15$ Mag. The extinction-marginalized likelihood distribution (dashed black line in Fig. 14) includes two well separated peaks located at $E_{B-V} = 0.026$ Mag and $E_{B-V} = 0.21$ Mag, and $E_{B-V} = 0.15$ Mag is the minimum between them. When limiting the extinction-prior to $0.047 \leq E_{B-V} \leq 0.15$ Mag the solu-

Table 8. PTF12gnt Likelihood local maxima $0.046 \leq E_{B-V} \leq 0.26$ Mag

Parameter	Peak #1	Peak #2	Peak #3	Peak #4	Peak #5	Peak #6	Peak #7
R_* [R_\odot]	2000_{-1372}^{+0}	414_{-54}^{+598}	421_{-61}^{+591}	420_{-60}^{+592}	460_{-101}^{+551}	2000_{-1372}^{+0}	406_{-46}^{+606}
$v_{s*,8.5}$	$0.93_{-0.24}^{+0.08}$	$1.45_{-0.63}^{+0.16}$	$1.44_{-0.63}^{+0.16}$	$1.44_{-0.63}^{+0.16}$	$1.19_{-0.44}^{+0.00}$	$0.78_{-0.09}^{+0.23}$	$1.17_{-0.42}^{+0.00}$
M_{ej} [M_\odot]	$2.6_{-0.6}^{+3.8}$	$2.2_{-0.2}^{+4.1}$	$2.2_{-0.2}^{+4.1}$	$2.2_{-0.2}^{+4.1}$	$4.2_{-2.2}^{+2.1}$	$2.0_{-0.0}^{+4.3}$	$2.3_{-0.3}^{+4.1}$
t_{ref} [MJD]	$56111.30_{-0.60}^{+0.03}$	$56111.20_{-0.50}^{+0.13}$	$56111.19_{-0.49}^{+0.13}$	$56111.20_{-0.50}^{+0.13}$	$56111.10_{-0.40}^{+0.23}$	$56111.31_{-0.61}^{+0.02}$	$56111.03_{-0.33}^{+0.29}$
f_ρ	$0.577_{-0.000}^{+0.464}$	$0.577_{-0.000}^{+0.464}$	$0.579_{-0.001}^{+0.462}$	$0.577_{-0.000}^{+0.464}$	$0.577_{-0.000}^{+0.464}$	$1.840_{-1.176}^{+1.323}$	$1.338_{-0.674}^{+1.825}$
E_{B-V}	$0.208_{-0.151}^{+0.003}$	$0.053_{-0.007}^{+0.048}$	$0.054_{-0.008}^{+0.047}$	$0.055_{-0.008}^{+0.047}$	$0.050_{-0.004}^{+0.051}$	$0.209_{-0.151}^{+0.003}$	$0.047_{-0.000}^{+0.055}$
χ^2/dof	33.63/ 21	33.24/ 20	33.28/ 20	33.28/ 20	49.44/ 27	75.11/ 47	51.28/ 27
	Peak #8	Peak #9	Peak #10	Peak #11	Peak #12	Peak #13	
R_* [R_\odot]	405_{-46}^{+606}	406_{-47}^{+605}	406_{-46}^{+606}	643_{-284}^{+368}	999_{-640}^{+13}	643_{-284}^{+368}	
$v_{s*,8.5}$	$1.17_{-0.42}^{+0.00}$	$1.17_{-0.42}^{+0.00}$	$1.17_{-0.42}^{+0.00}$	$0.85_{-0.16}^{+0.16}$	$0.74_{-0.04}^{+0.28}$	$0.85_{-0.16}^{+0.16}$	
M_{ej} [M_\odot]	$2.3_{-0.3}^{+4.1}$	$4.1_{-2.1}^{+2.2}$	$2.2_{-0.2}^{+4.1}$	$2.8_{-0.8}^{+3.5}$	$3.5_{-1.5}^{+2.8}$	$2.5_{-0.5}^{+3.8}$	
t_{ref} [MJD]	$56111.04_{-0.34}^{+0.28}$	$56111.03_{-0.33}^{+0.29}$	$56111.04_{-0.34}^{+0.29}$	$56110.97_{-0.27}^{+0.35}$	$56110.96_{-0.26}^{+0.37}$	$56111.30_{-0.60}^{+0.03}$	
f_ρ	$1.342_{-0.678}^{+1.821}$	$0.740_{-0.162}^{+0.301}$	$1.353_{-0.689}^{+1.809}$	$3.162_{-2.498}^{+0.000}$	$3.073_{-2.409}^{+0.090}$	$0.577_{-0.000}^{+0.464}$	
E_{B-V}	$0.047_{-0.000}^{+0.055}$	$0.047_{-0.000}^{+0.055}$	$0.047_{-0.000}^{+0.055}$	$0.049_{-0.002}^{+0.052}$	$0.091_{-0.044}^{+0.011}$	$0.210_{-0.152}^{+0.001}$	
χ^2/dof	51.28/ 27	51.29/ 27	51.29/ 27	65.23/ 37	88.85/ 51	1418.86/ 27	

Table 9. PTF12gnt Likelihood local maxima $0.046 \leq E_{B-V} \leq 0.15$ Mag

Parameter	Peak #1	Peak #2	Peak #3	Peak #4	Peak #5
R_* [R_\odot]	418_{-2}^{+403}	455_{-34}^{+367}	236_{-0}^{+512}	491_{-71}^{+330}	382_{-0}^{+404}
$v_{s*,8.5}$	$1.43_{-0.65}^{+0.00}$	$1.39_{-0.62}^{+0.00}$	$1.84_{-1.03}^{+0.16}$	$1.21_{-0.48}^{+0.00}$	$1.25_{-0.51}^{+0.00}$
M_{ej} [M_\odot]	$2.2_{-0.2}^{+5.2}$	$2.2_{-0.2}^{+5.2}$	$2.0_{-0.0}^{+5.5}$	$3.7_{-1.7}^{+3.8}$	$2.8_{-0.8}^{+4.7}$
t_{ref} [MJD]	$56111.20_{-0.44}^{+0.00}$	$56111.20_{-0.44}^{+0.00}$	$56111.20_{-0.44}^{+0.00}$	$56111.10_{-0.35}^{+0.09}$	$56111.10_{-0.35}^{+0.09}$
f_ρ	$0.577_{-0.000}^{+0.575}$	$0.577_{-0.000}^{+0.575}$	$0.577_{-0.000}^{+0.575}$	$0.577_{-0.000}^{+0.575}$	$0.883_{-0.306}^{+0.269}$
E_{B-V}	$0.052_{-0.006}^{+0.027}$	$0.055_{-0.008}^{+0.024}$	$0.050_{-0.003}^{+0.029}$	$0.055_{-0.008}^{+0.024}$	$0.047_{-0.000}^{+0.033}$
χ^2/dof	33.37/ 20	33.89/ 20	27.62/ 14	49.93/ 27	50.92/ 27
	Peak #6	Peak #7	Peak #8	Peak #9	Peak #10
R_* [R_\odot]	400_{-0}^{+402}	636_{-216}^{+185}	418_{-2}^{+403}	436_{-16}^{+385}	1000_{-457}^{+0}
$v_{s*,8.5}$	$1.16_{-0.45}^{+0.00}$	$0.86_{-0.22}^{+0.17}$	$1.12_{-0.43}^{+0.00}$	$1.06_{-0.39}^{+0.00}$	$0.75_{-0.10}^{+0.28}$
M_{ej} [M_\odot]	$3.0_{-1.0}^{+4.5}$	$3.0_{-1.0}^{+4.5}$	$3.3_{-1.3}^{+4.1}$	$2.0_{-0.0}^{+5.5}$	$3.7_{-1.7}^{+3.8}$
t_{ref} [MJD]	$56111.00_{-0.25}^{+0.19}$	$56111.00_{-0.25}^{+0.19}$	$56111.00_{-0.25}^{+0.19}$	$56111.00_{-0.25}^{+0.19}$	$56110.90_{-0.15}^{+0.29}$
f_ρ	$1.018_{-0.440}^{+0.135}$	$2.744_{-2.079}^{+0.027}$	$1.018_{-0.440}^{+0.135}$	$2.744_{-2.079}^{+0.027}$	$2.382_{-1.717}^{+0.389}$
E_{B-V}	$0.047_{-0.000}^{+0.033}$	$0.048_{-0.001}^{+0.031}$	$0.047_{-0.000}^{+0.033}$	$0.047_{-0.000}^{+0.033}$	$0.090_{-0.037}^{+0.007}$
χ^2/dof	52.06/ 27	65.25/ 37	52.41/ 27	53.21/ 27	89.67/ 51

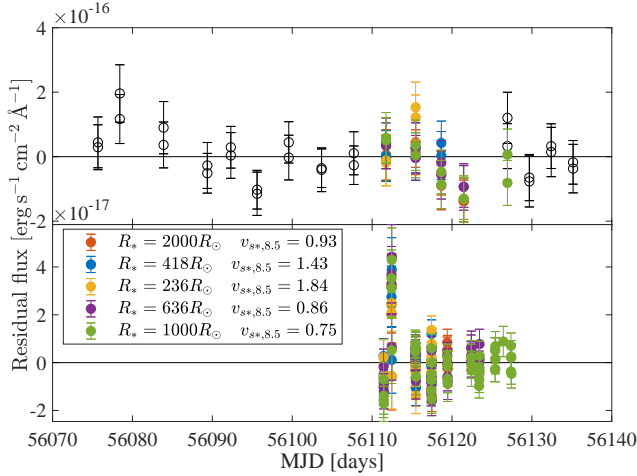
tions with progenitor radius greater than $1000R_\odot$ disappear (solid black contour on Fig. 13) and the secondary peak in t_{ref} (dashed and solid black lines in Fig. 14) disappears as well. The maximal likelihood solutions with narrowed extinction prior (Table 9, plus black markers on Fig. 13) are not located in a single peak like PTF12ffs but include several sub-peaks. The left cluster of solutions is characterized by higher progenitor radii ($500-1000R_\odot$) and lower shock velocity parameter. The solutions in this cluster include a non negligible likelihood for all the f_ρ values. The right cluster of solutions is characterized by lower progenitor radii ($350-700R_*$) and higher shock velocity parameter values. The solu-

tions in this cluster have a significant likelihood only for f_ρ values smaller than 1.2. Although the likelihood of the individual solutions in the right cluster have a higher likelihood than the ones in the left cluster (see Table 9), the marginalized distributions for R_* and v_{s*} , which are a result of an integral over all of the f_ρ values have a higher likelihood values than those of the left cluster solutions.

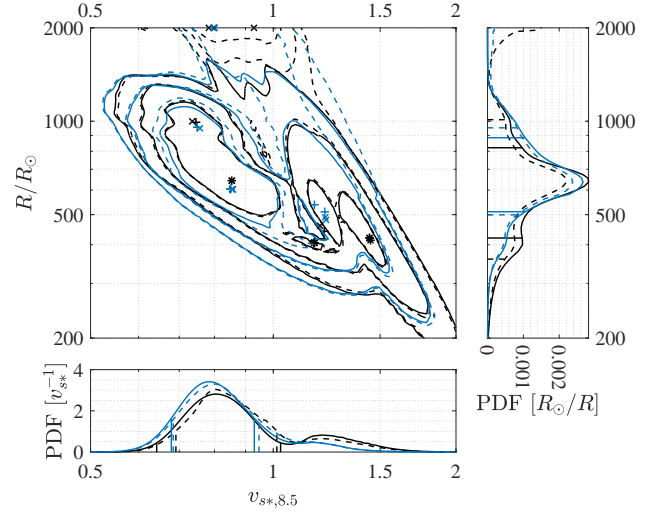
All of the solutions for the SN have a χ^2/dof ratio of 1.5 – 1.8 which is worse than the ratio we receive for the other SNe. Examining the light curve (Figure 11) and the best-fit residuals (Fig. 12) we see that the R -band measurements from the first night of the SN detection

Table 10. PTF12gnt Likelihood local maxima, without 3 R data points, $0.046 \leq E_{B-V} \leq 0.26$ Mag

Parameter	Peak #1	Peak #2	Peak #3	Peak #4
$R_* [R_\odot]$	481^{+455}_{-0}	490^{+454}_{-0}	604^{+349}_{-105}	603^{+350}_{-104}
$v_{s*,8.5}$	$1.22^{+0.00}_{-0.46}$	$1.22^{+0.00}_{-0.45}$	$0.85^{+0.09}_{-0.17}$	$0.86^{+0.09}_{-0.17}$
$M_{ej} [M_\odot]$	$3.4^{+5.4}_{-1.4}$	$3.4^{+5.4}_{-1.4}$	$3.1^{+5.6}_{-1.1}$	$3.1^{+5.7}_{-1.1}$
$t_{ref} [\text{MJD}]$	$56111.23^{+0.10}_{-0.44}$	$56111.23^{+0.10}_{-0.43}$	$56111.11^{+0.22}_{-0.32}$	$56111.12^{+0.21}_{-0.32}$
f_ρ	$0.596^{+0.719}_{-0.019}$	$0.594^{+0.721}_{-0.017}$	$3.161^{+0.002}_{-2.416}$	$3.161^{+0.001}_{-2.416}$
E_{B-V}	$0.048^{+0.042}_{-0.001}$	$0.051^{+0.039}_{-0.005}$	$0.047^{+0.043}_{-0.000}$	$0.047^{+0.043}_{-0.000}$
χ^2/dof	24.83/ 22	24.87/ 22	35.77/ 34	35.82/ 34
	Peak #5	Peak #6	Peak #7	Peak #8
$R_* [R_\odot]$	2000^{+0}_{-1361}	2000^{+0}_{-1361}	2000^{+0}_{-1361}	949^{+3}_{-450}
$v_{s*,8.5}$	$0.80^{+0.15}_{-0.12}$	$0.80^{+0.15}_{-0.11}$	$0.80^{+0.15}_{-0.11}$	$0.76^{+0.19}_{-0.07}$
$M_{ej} [M_\odot]$	$4.0^{+4.8}_{-2.0}$	$4.0^{+4.8}_{-2.0}$	$2.4^{+6.3}_{-0.4}$	$14.2^{+0.8}_{-10.6}$
$t_{ref} [\text{MJD}]$	$56111.58^{+0.00}_{-0.68}$	$56111.58^{+0.00}_{-0.68}$	$56111.59^{+0.00}_{-0.69}$	$56111.10^{+0.23}_{-0.31}$
f_ρ	$0.890^{+0.425}_{-0.312}$	$0.886^{+0.429}_{-0.308}$	$1.602^{+0.192}_{-0.970}$	$0.577^{+0.738}_{-0.000}$
E_{B-V}	$0.232^{+0.001}_{-0.172}$	$0.230^{+0.000}_{-0.170}$	$0.233^{+0.007}_{-0.173}$	$0.090^{+0.005}_{-0.042}$
χ^2/dof	55.03/ 45	55.05/ 45	55.05/ 45	60.25/ 48

**Figure 12.** PTF12gnt best-fit residuals for the models plotted in Fig. 11. The upper panel shows the NUV band residuals and the bottom panel is for the R band ones. The color code is the same as in Fig. 7. The empty black circles are the residuals of the NUV background estimation.

are spread along a large range of flux values. All the solutions (Tables 8 and 9) agree with the lowest flux point measured and fail to match the higher flux values during this night. Those points introduce an error of about 10 in χ^2 units for all the solutions, leading to this unusual goodness of fit ratio. Since the χ^2 distribution has the highest slope when $\chi^2 \sim \nu$, where ν is the number of degrees of freedom, the effect of those points on models with higher likelihood (i.e. $\chi^2 \sim \nu$) is larger than their effect on models with lower likelihood. When we ignore these three measurements and treat them as outliers, we get better goodness of fit scores as presented in Tables 10 and 11. Those scores are similar to the ones we get

**Figure 13.** PTF12gnt R_* - v_{s*} likelihood map. The solid contour lines represents 1σ , 2σ and 3σ of the cumulative likelihood with an extinction prior of $0.047 \leq E_{B-V} \leq 0.15$ Mag, and the dashed contour represents the cumulative likelihood with a prior of $0.047 \leq E_{B-V} \leq 0.26$ Mag. The plus markers indicate a maximal likelihood models with the first prior while the cross symbols are for the maximal likelihood models with the second prior (Asterisks are just plus and cross markers on the same spot and not a separate marker). The bottom and right panels show the marginal distributions for v_{s*} and R_* where the solid line plot the marginal distribution with the first prior and the dashed ones with the second prior. The black lines and symbols are the likelihood distributions and results when all the R band data points were taken into account, and the blue ones represent the results when three suspicious R band data points were treated as outliers.

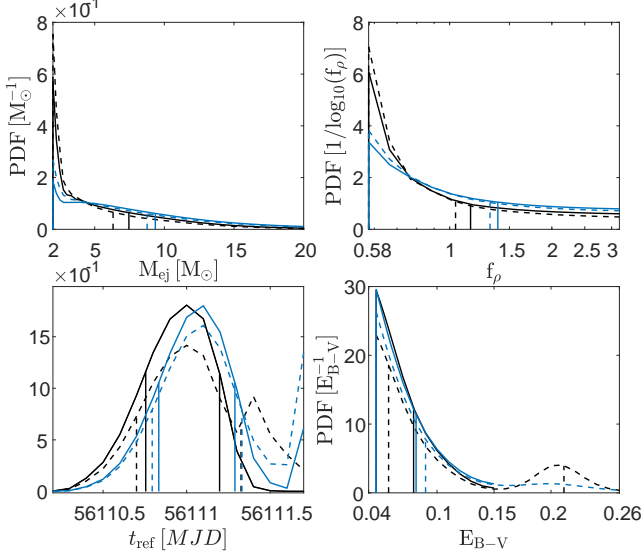


Figure 14. PTF12gnt Marginal distributions for M_{ej} , f_{ρ} , t_{ref} and E_{B-V} . Solid lines represent the marginal distributions with an extinction prior of up to 0.15 Mag while the dashed ones plot the distributions with a prior of up to 0.26 Mag. The black lines stand for the likelihood distributions when all the R band data points were taken into account, and the blue ones represent the results when three suspicious R band data points were treated as outliers.

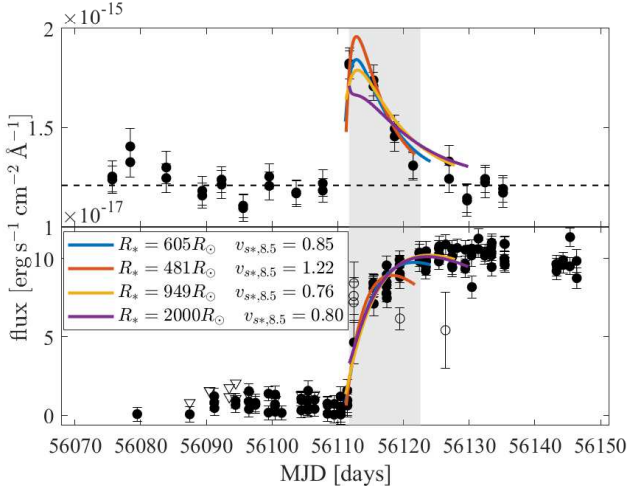


Figure 15. PTF12gnt data points and best-fitting models when the suspicious three R band-data points were treated as outliers. The same symbol convention as in Fig 11 is used. The model full parameters are listed in Tables 10 and 11.

for the other SNe. Removing those points also changes the marginalized progenitor radius likelihood (Blue contours in Fig. 13) and suppresses the secondary peaks at $\sim 2000R_{\odot}$ and $R_{*} \sim 400R_{\odot}$. We still find a correlation between the $R_{*} \sim 2000R_{\odot}$ solutions and the extinction values larger than $E_{B-V} = 0.15$ Mag and present the results with a narrower extinction prior. Selected solu-

Table 11. PTF12gnt Likelihood local maxima, without 3 R data points, $0.046 \leq E_{B-V} \leq 0.15$ Mag

Parameter	Peak #1	Peak #2
R_{*} [R_{\odot}]	511^{+374}_{-0}	538^{+347}_{-27}
$v_{s*,8.5}$	$1.22^{+0.00}_{-0.46}$	$1.17^{+0.00}_{-0.42}$
M_{ej} [M_{\odot}]	$2.5^{+6.9}_{-0.5}$	$3.0^{+6.3}_{-1.0}$
t_{ref} [MJD]	$56111.23^{+0.06}_{-0.40}$	$56111.18^{+0.11}_{-0.35}$
f_{ρ}	$0.736^{+0.651}_{-0.158}$	$0.711^{+0.676}_{-0.133}$
E_{B-V}	$0.053^{+0.029}_{-0.006}$	$0.066^{+0.016}_{-0.019}$
χ^2/dof	25.04/ 22	26.82/ 24

Parameter	Peak #3	Peak #4
R_{*} [R_{\odot}]	605^{+280}_{-94}	956^{+0}_{-396}
$v_{s*,8.5}$	$0.85^{+0.08}_{-0.17}$	$0.75^{+0.18}_{-0.07}$
M_{ej} [M_{\odot}]	$3.2^{+6.1}_{-1.2}$	$14.6^{+0.0}_{-10.7}$
t_{ref} [MJD]	$56111.11^{+0.18}_{-0.28}$	$56111.09^{+0.20}_{-0.25}$
f_{ρ}	$3.162^{+0.000}_{-2.397}$	$0.577^{+0.809}_{-0.000}$
E_{B-V}	$0.047^{+0.035}_{-0.000}$	$0.091^{+0.001}_{-0.041}$
χ^2/dof	35.72/ 34	60.55/ 48

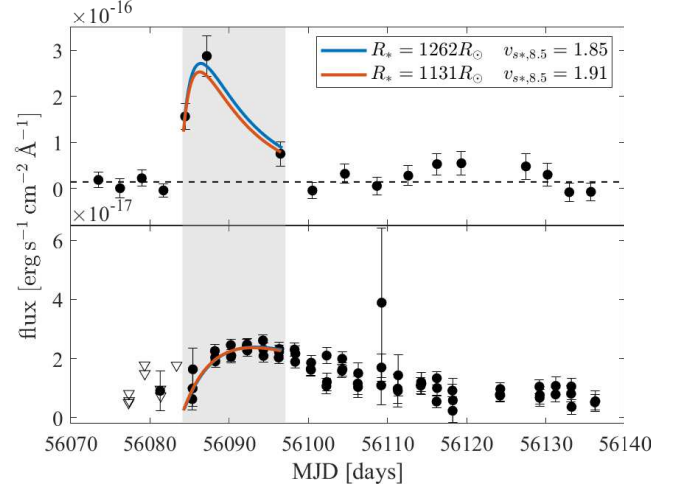


Figure 16. PTF12fkp data points and best-fitting models. The upper panel describes the NUV band data and the lower one is for the R band. The dashed horizontal line in the top panel represents the measured NUV background. The triangles in the bottom panel stand for 3σ limits. The colored lines show the different solutions. The R_{*} and v_{s*} values of these solutions are list in the legend, while the other parameters are listed in Table 12. The grayed background area indicates the NUV transient. NUV data points external to this area were used to calculate the NUV background.

tions from Tables 10 and 11 are plotted against the data in Figure 15. We see that while all the solutions match the R -band data points well, the $R_{*} = 2000R_{\odot}$ solution does not match the early NUV data points.

4.3. PTF12fkp

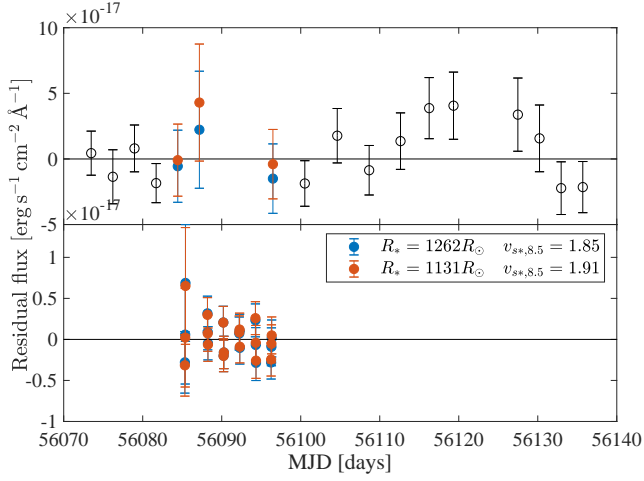


Figure 17. PTF12fkp best-fit residuals for the models plotted in Fig. 16. The upper panel shows the *NUV* band residuals and the lower panel the *R* band ones. The color code is the same as in Fig. 16. The empty black circles are the residuals of the *NUV* background estimation.

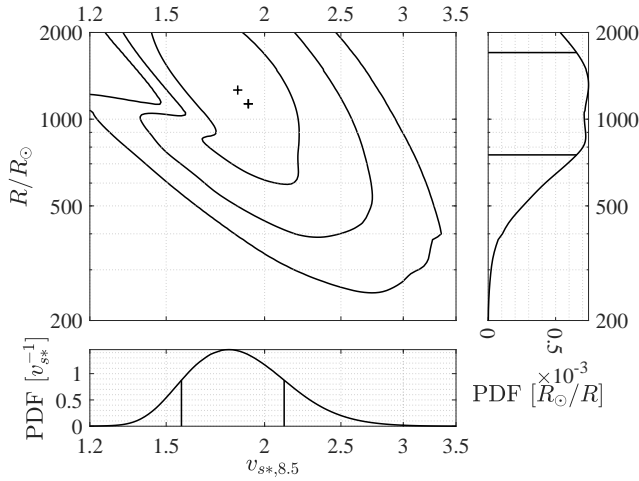


Figure 18. PTF12fkp R_* - v_{s*} likelihood map. The solid contour lines represents 1σ , 2σ and 3σ of the cumulative likelihood. The plus markers mark the maximal likelihood models. The bottom and right panels show the marginalized distributions for v_{s*} and R_* .

PTF12fkp data points together with its most likely models appear in Figure 16, while the most likely best-fit residuals are presented in Figure 17. The marginalized R_* - v_{s*} likelihood map and the marginalized likelihood for each parameter are plotted in Figure 18 and the marginalized likelihood distributions for M_{ej} , f_ρ , t_{ref} and E_{B-V} are shown in Figure 19. The local maxima of the likelihood are listed in Table 12 and marked in Figure 17 by plus symbols.

The PTF12fkp *NUV* data includes a measurement during the rise of the flux to its maximum, and our

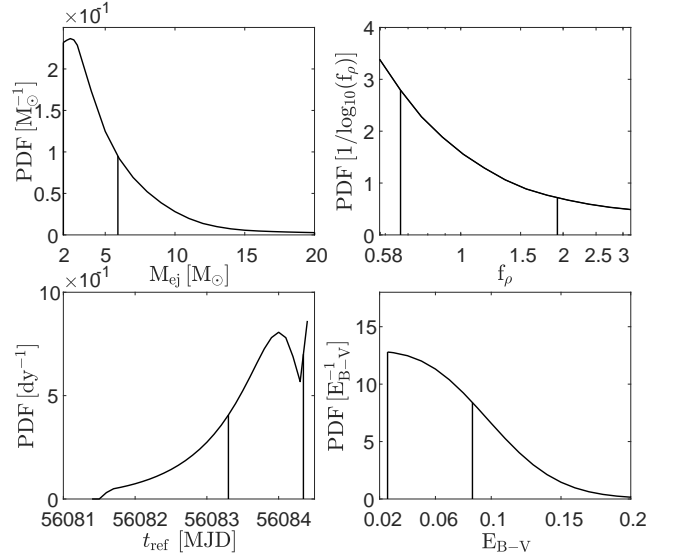


Figure 19. PTF12fkp marginal distribution for M_{ej} , f_ρ , t_{ref} and E_{B-V} .

Table 12. PTF12fkp Likelihood local maxima

Parameter	Peak #1	Peak #2
$R_* [R_\odot]$	1262_{-511}^{+441}	1131_{-379}^{+572}
$v_{s*,8.5}$	$1.85_{-0.28}^{+0.27}$	$1.91_{-0.34}^{+0.21}$
$M_{\text{ej}} [M_\odot]$	$2.1_{-0.1}^{+3.8}$	$2.0_{-0.0}^{+3.9}$
$t_{\text{ref}} [\text{MJD}]$	$56084.20_{-0.90}^{+0.14}$	$56084.11_{-0.81}^{+0.24}$
f_ρ	$1.824_{-1.158}^{+0.101}$	$2.175_{-1.428}^{+0.987}$
E_{B-V}	$0.026_{-0.000}^{+0.061}$	$0.032_{-0.006}^{+0.055}$
χ^2/dof	12.90/ 14	13.06/ 14

solutions fit this data point very well (Figure 16). Its *NUV* data suffer from a significant loss during the decay of the signal from its peak. Like the other SNe, the marginal progenitor radius likelihood distribution (Fig. 18) has non-negligible values for large values of $2000R_\odot$. Unlike the previous SNe, we did not find any dual peak structure in the extinction marginalized likelihood distributions (Fig. 19) which allow us to limit our prior and to suppress the likelihood of these large radius models. While the solutions we find (Tab. 12) fit the data very well, the limits we receive for the radius are very wide. If some of the *NUV* data points were not lost, we may have had a better constraints on the radius.

4.4. PTF12ftc

PTF12ftc data points together with its most likely models appear in Figure 20, while the most likely best-fit residuals are presented in Figure 21. The marginalized R_* - v_{s*} likelihood map and the marginalized likelihood for each parameter are plotted in Figure 22 and the marginalized likelihood distributions M_{ej} , f_ρ , t_{ref}

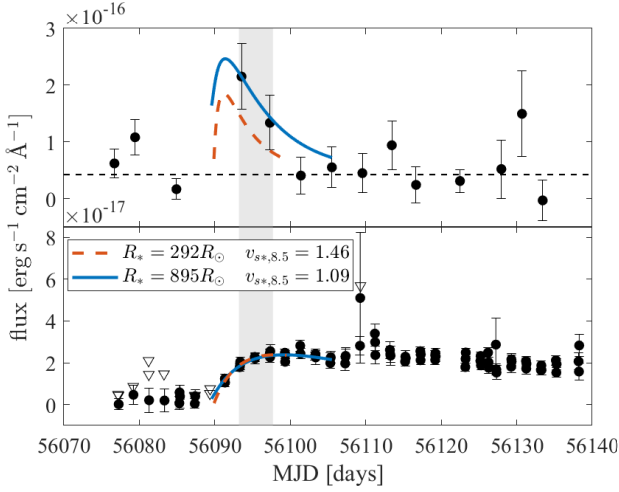


Figure 20. PTF12ftc data points and best fitting models. The upper panel describes the *NUV* band data and the lower one is for the *R* band. The dashed horizontal line in the top panel represents measured *NUV* background. The triangles in the bottom stand for 3σ limits. The colored lines show the different solutions. The R_* and v_{s*} values of these solution are listed in the legend, while the other parameters are in Table 13. The grayed background area marks the *NUV* transient. Data points external to this area were used to calculate the *NUV* background.

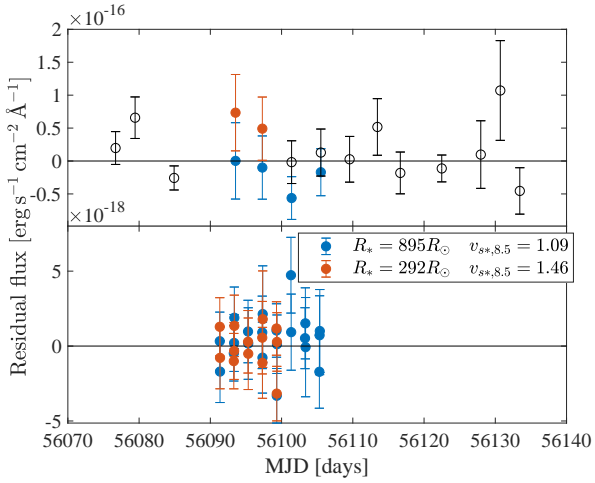


Figure 21. PTF12ftc best-fits residuals for the models plotted on Fig. 20. The top panel shows the *NUV* band residuals and the bottom panel the *R* band ones. The color code is the same as in Fig. 20. The empty black circles are the residuals of the *NUV* background estimation.

and E_{B-V} are shown in Figure 23. The local maxima of the likelihood are listed in Table 13 and marked on Figure 21 by plus symbols.

While all the three solution in Table 13 are in good agreement with the *R*-band readings, the solutions with the lower progenitor radius ($\sim 300R_\odot$) do not match the

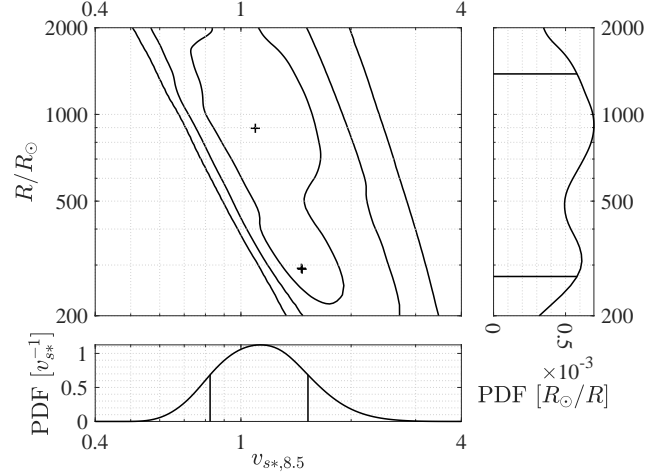


Figure 22. PTF12ftc R_* - v_{s*} likelihood map. The solid contour lines represents 1σ , 2σ and 3σ of the cumulative likelihood. The plus markers indicate the maximal likelihood solutions. The bottom and right panels show the marginal distributions for v_{s*} and R_* .

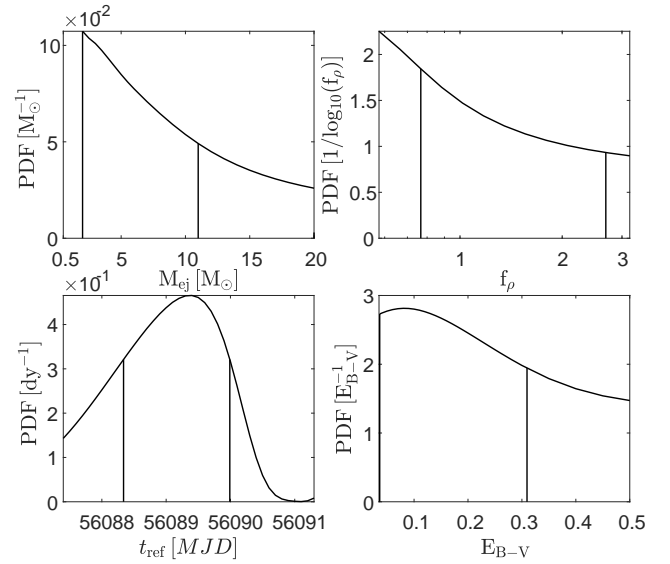


Figure 23. PTF12ftc marginal distributions for M_{ej} , f_ρ , t_{ref} and E_{B-V} .

NUV data points (see Figs. 20 and 21 for a comparison of the solutions against the data). This anomaly is a result of the small amount of data points these solution are valid for. In addition these solutions are dominated by the *R*-band points (these solutions are valid for two *NUV*-band points and ten *R*-band points). The good match to the *R*-band points covers for the mismatch with the *NUV* points, leading to an overall reasonable goodness of fit score. However, since we require a solution to match well all the different bands in addition to its overall goodness of fit score, we reject these solu-

Table 13. PTF12ftc Likelihood local maxima

Parameter	Peak #1 ^a	Peak #2 ^a	Peak #3
R_* [R_\odot]	292^{+1090}_{-19}	290^{+1092}_{-17}	895^{+487}_{-621}
$v_{s*,8.5}$	$1.46^{+0.06}_{-0.64}$	$1.47^{+0.05}_{-0.65}$	$1.09^{+0.43}_{-0.27}$
M_{ej} [M_\odot]	$4.4^{+6.6}_{-2.4}$	$4.9^{+6.1}_{-2.9}$	$2.0^{+9.0}_{-0.0}$
t_{ref} [MJD]	$56089.86^{+0.13}_{-1.52}$	$56089.85^{+0.14}_{-1.51}$	$56089.49^{+0.50}_{-1.15}$
f_ρ	$2.229^{+0.153}_{-1.506}$	$1.867^{+0.157}_{-1.202}$	$2.395^{+0.293}_{-1.628}$
E_{B-V}	$0.036^{+0.273}_{-0.000}$	$0.036^{+0.273}_{-0.000}$	$0.038^{+0.272}_{-0.001}$
χ^2/dof	4.62/ 6	4.63/ 6	13.00/ 15

^a These solutions have a poor match to the NUV data points (see Figs. 20 and 21) and should be rejected.

tions. We report them since our SOPRANOS tool found them as possible solutions. The *NUV* data of this SN suffers from a data loss between the last non-detection and the first detection of the SN. The marginal distribution for the extinction has a non-negligible likelihood even for very high values of E_{B-V} . The progenitor radius for this SN has poor limits which may be a result of the small amount of *NUV* data points the solutions are valid for. Examining the marginal distributions for the other model parameters (Fig. 23) we did not find any secondary peaks which may have a correlation with the $\gtrsim 1000R_\odot$ progenitor radius models. If we have found such a correlation we could narrow down our prior to avoid the non-physical large progenitor radius values. If we set a requirement of a minimal number of 13 valid data points (7 degrees of freedom), the low radii solutions ($\sim 300R_\odot$) disappear, leading to a tighter progenitor radius limit.

4.5. PTF12fzhz

PTF12fzhz data points together with its most likely models appear in Figure 24, while the most likely best-fit residuals are presented in Figure 25. The marginalized R_* - v_{s*} likelihood map and the marginalized likelihood for each parameter are plotted in Figure 26 and the marginalized likelihood distributions M_{ej} , f_ρ , t_{ref} and E_{B-V} are shown in Figure 27. The local maxima of the likelihood are listed in Table 14 and marked on Figure 25 by plus symbols.

The *R*-band light curve (Figure 24) shows a dual peak structure, which is common to type IIb SNe, like PTF12fzhz. SW17 have shown that their model can explain the first peak of the two when extending the f_ρ prior to values smaller than $\sqrt{1/3}$. Following SW17, as mentioned in §3.5, we extended our f_ρ prior to include values starting from 0.1. Like the Sapir & Waxman (2017) results for LSQ14bdq and 1993J, our solutions for PTF12fzhz converge to low radius progenitor $R_* < 300R_\odot$ and low f_ρ value. Here we show that the model

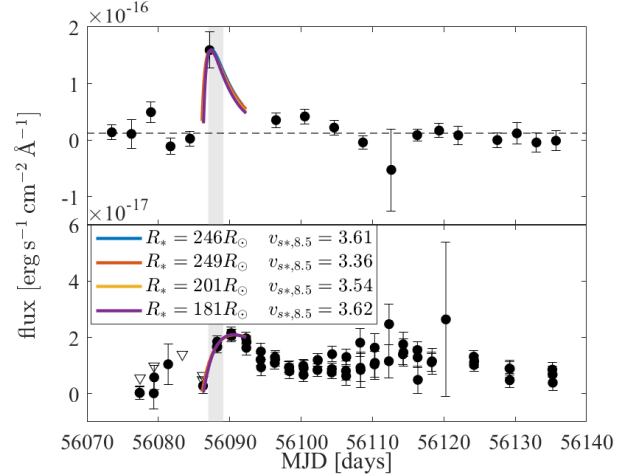


Figure 24. PTF12fzhz data points and best-fitting models. The upper panel describes the *NUV* band data and the lower one is for the *R* band. The dashed horizontal line in the top panel represents the measured *NUV* background. The triangles in the bottom panel stand for 3σ limits. The colored lines show the different solutions. The R_* and v_{s*} values for these solutions are listed in the legend, while the other parameters are in Table 14. The grayed background area marks the *NUV* transient. Data points external to this area were used to calculate the *NUV* background.

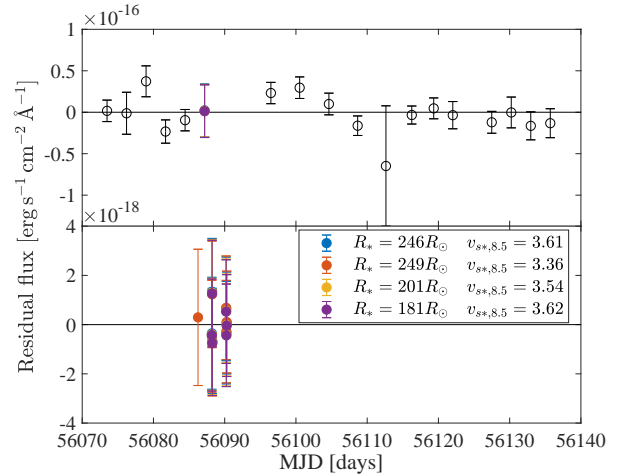


Figure 25. PTF12fzhz best-fits residuals for the models plotted on Fig. 24. The upper panel shows the *NUV* band residuals and the bottom panel the *R* band. The color code is the same as in Fig. 24. The empty black circles are the residuals of the *NUV* background estimation.

also matches the *NUV* band data. Such low radius solutions are valid only for a short period of time, and our low cadence survey has obtained only a small number of data points during the models validity period. Our most likely models are valid for small number of 7-11 data points in the two bands together. While the solutions

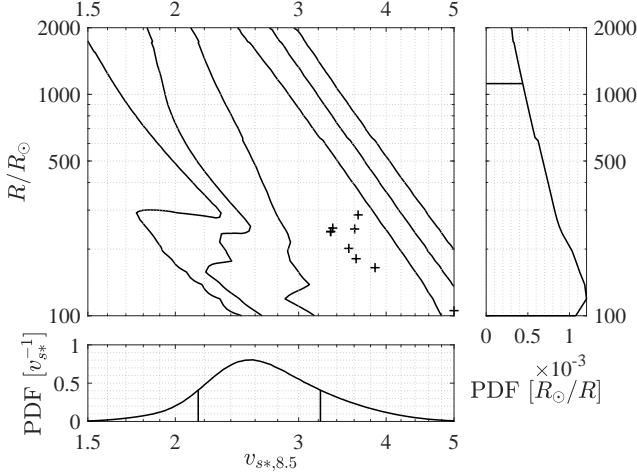


Figure 26. PTF12fzh R_* - v_{s*} likelihood map. The solid contour lines represents 1σ , 2σ and 3σ of the cumulative likelihood. The plus markers indicate the maximal likelihood models. The bottom and right panels show the marginal distributions for v_{s*} and R_* .

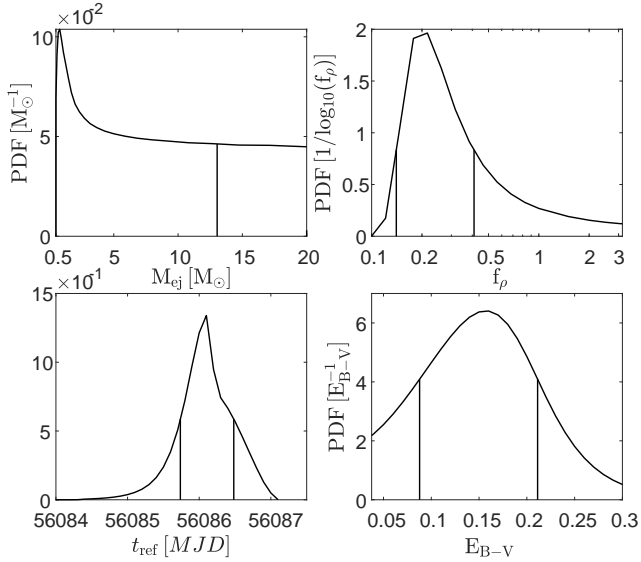


Figure 27. PTF12fzh marginal distributions for M_{ej} , f_ρ , t_{ref} and E_{B-V} .

have a good goodness of fit, the very small number of data points they are valid for makes the statistical significance of this result poor. We cannot place a tight limit on the progenitor radius. Its marginal likelihood distribution decays slowly towards $2000R_\odot$ and beyond. This result may be explained by the fact that we have only one valid *NUV* point, and few data points in epochs following it were lost. The ejecta mass marginal likelihood distribution has a peak at $2M_\odot$ and then has a non-zero asymptotic value (Figure 27). This can be explained by our solutions having small f_ρ values and that Eq. 3 de-

Table 14. PTF12fzh Likelihood local maxima

Parameter	Peak #1	Peak #2	Peak #3
R_* [R_\odot]	246^{+872}_{-146}	201^{+917}_{-101}	181^{+937}_{-81}
$v_{s*,8.5}$	$3.61^{+0.00}_{-1.24}$	$3.54^{+0.00}_{-1.19}$	$3.62^{+0.00}_{-1.25}$
M_{ej} [M_\odot]	$1.5^{+11.5}_{-1.0}$	$4.7^{+8.4}_{-4.2}$	$5.7^{+7.4}_{-5.2}$
t_{ref} [MJD]	$56086.23^{+0.25}_{-0.50}$	$56086.24^{+0.25}_{-0.50}$	$56086.29^{+0.19}_{-0.56}$
f_ρ	$0.902^{+0.000}_{-0.716}$	$0.447^{+0.000}_{-0.297}$	$0.401^{+0.009}_{-0.260}$
E_{B-V}	$0.098^{+0.114}_{-0.010}$	$0.082^{+0.124}_{-0.000}$	$0.077^{+0.125}_{-0.000}$
χ^2/dof	0.60/ 1	0.60/ 1	0.60/ 1
Parameter	Peak #4	Peak #5	Peak #6
R_* [R_\odot]	165^{+954}_{-65}	240^{+878}_{-140}	249^{+869}_{-149}
$v_{s*,8.5}$	$3.86^{+0.00}_{-1.42}$	$3.33^{+0.00}_{-1.09}$	$3.36^{+0.00}_{-1.10}$
M_{ej} [M_\odot]	$5.1^{+7.9}_{-4.6}$	$10.3^{+2.8}_{-9.8}$	$2.5^{+10.6}_{-2.0}$
t_{ref} [MJD]	$56086.40^{+0.08}_{-0.67}$	$56086.23^{+0.25}_{-0.50}$	$56086.06^{+0.42}_{-0.33}$
f_ρ	$0.403^{+0.007}_{-0.262}$	$0.271^{+0.139}_{-0.131}$	$0.684^{+0.000}_{-0.507}$
E_{B-V}	$0.077^{+0.125}_{-0.000}$	$0.087^{+0.123}_{-0.000}$	$0.089^{+0.122}_{-0.002}$
χ^2/dof	0.60/ 1	0.61/ 1	0.61/ 2
Parameter	Peak #7	Peak #8	
R_* [R_\odot]	286^{+833}_{-186}	105^{+1013}_{-5}	
$v_{s*,8.5}$	$3.65^{+0.00}_{-1.27}$	$5.00^{+0.00}_{-2.48}$	
M_{ej} [M_\odot]	$7.3^{+5.7}_{-6.8}$	$6.4^{+6.6}_{-5.9}$	
t_{ref} [MJD]	$56086.12^{+0.36}_{-0.39}$	$56086.13^{+0.35}_{-0.40}$	
f_ρ	$0.362^{+0.047}_{-0.222}$	$0.483^{+0.000}_{-0.328}$	
E_{B-V}	$0.198^{+0.013}_{-0.110}$	$0.234^{+0.000}_{-0.129}$	
χ^2/dof	4.68/ 3	10.54/ 5	

pends on the multiplication of f_ρ and M_{ej} . For a small f_ρ value, a small absolute change is a large relative change. In order to maintain the value of the multiplication of the two, M_{ej} value should be changed by an inverse factor, which leads to large change of its absolute value. While the different solutions range $M_{ej} = 1.5 - 10.3M_\odot$ and $f_\rho = 0.27 - 0.9$ their multiplication is in the limited range of $f_\rho M_{ej} = 1.4 - 2.7M_\odot$.

5. DISCUSSION

A phenomenon we encountered which is of general relevance is that when we fit SW17 models to the data, we find a preference for large progenitor radii ($\gtrsim 1000R_\odot$). The reason for this preference is that large radius models become valid at late times (Equation 5), typically after the *NUV* signal is no longer significant. When we use the MSW20 extension to the SW17 model, the early *NUV* data points became valid for all models, and we find that progenitor radii of few hundreds of solar radii have higher likelihood than the $R_* \gtrsim 1000R_\odot$ solutions. This is important to account for when applying either the RW11 or the SW17 models to observations.

The marginalized progenitor-radius likelihood distributions of all the analyzed SNe have a non-negligible

likelihood for presumably non-physical progenitor radii of about $2000R_{\odot}$. For PTF12ffs and PTF12gnt, where we have many data points in both *NUV* and *R*-bands we have recognized a correlation between these large radius solutions and a secondary peak in the marginalized extinction distribution, with a higher extinction value. This is explained by Equations 3 and 11. When we limit the prior on the extinction values to include only the peak with lower extinction values for those SNe, the high radius solutions disappear. For the other SNe, for which we obtained fewer data points and only a few *NUV* data points with values larger than their *NUV* background, we do not identify a secondary peak in any of the other parameters marginalized distributions. This behaviour may be explained by the small number of data points within the model validity period and the characteristics of the χ^2 probability density function for small number of degrees of freedom, which does not fall sharply from maximum at $\chi^2 \sim \nu$, resulting in a slow decay of the likelihood function from its maximum. Our work demonstrates the importance of constraining the extinction towards these events in order to properly derive their progenitor radii. The largest difference between the predicted light curves of best-fit models for PTF12gnt and PTF12ffs is at times where we do not have an *NUV*-band measurement. We believe that if we had a higher cadence in this band, data points in these times could differentiate better between the best-fit models, leading to a tighter constraint.

Whether or not we were able to achieve a tight constraint on the progenitor radius, all the solutions SOPRANOS converged to have an acceptable goodness of fit with the exception of PTF12gnt. For PTF12gnt we identify a group of three *R*-band measurements on the first night of the SN detection which do not match any model. While we do not have a statistical justification to ignore those data points, when we ignore them the solutions match the data well, and also suppress the likelihood of the nonphysical large radius solutions.

The light curves of PTF12gnt, PTF12fkp, and PTF12ftc demonstrate that the *NUV*-band data points are critical for narrowing the confidence intervals of the solutions. The double peaked SN PTF12fhz demonstrates that SW17 models are able to explain not only the first peak of the double peaked *R*-band light curve, but also its *NUV* behaviour.

We conclude the discussion by the fact that higher cadence *NUV* surveys, with higher measurement accuracy as expected to be conducted by the *ULTRASAT* space mission, would allow us to obtain a tight constraints on SN progenitor radii. This fact was shown by analysis in Rubin & Gal-Yam (2017).

6. CONCLUSION

We have developed SOPRANOS, a maximum likelihood fitting tool, which takes into account all the valid data points for each shock-cooling model and uses the likelihood function to compare between the different models. This is in contrast to previous works which used a constant set of data points for all the models, ignoring the validity time range of the models.

We have analyzed the SNe detected during the GALEX/PTF experiment using SOPRANOS, and found a good agreement between the MSW model and the data. The introduction of the MSW model extension allowed us to utilize all the early *NUV* data points. For two SNe with dense *NUV* data points we also achieved a good constraint on the progenitor radius. This constraint was achieved despite the low cadence of our survey. Higher cadence *NUV* surveys, such as *ULTRASAT*, will provide definitive measurements of the progenitor radii of core-collapse SNe.

We also have demonstrated that supergiant stars with small envelope to core ratio f_{ρ} may explain the double peaked type IIb SNe, as shown by Sapir & Waxman (2017), and that their solution is also compatible with the *NUV* band data points of PTF12fhz, complementing the visible light data analyzed by these authors.

ACKNOWLEDGMENTS

We want to thank Barak Zackay for useful discussions leading to the development of SOPRANOS formalism.

E.O.O. is grateful for the support by grants from the Israel Science Foundation, Minerva, Israeli Ministry of Technology and Science, the US-Israel Binational Science Foundation, Weizmann-UK, Weizmann-Yale, the Weizmann-Caltech grants, the Norman E. Alexander Family M. Foundation ULTRASAT Data Center Fund, Jonathan Beare, André Deloro Institute for Space and Optics Research, Schwartz/Reisman Collaborative Science Program and the Willner Family Leadership Institute for the Weizmann Institute of Science.

AGY's research is supported by the EU via ERC grant No. 725161, the ISF GW excellence center, an IMOS space infrastructure grant and BSF/Transformative and GIF grants, as well as The Benozio Endowment Fund for the Advancement of Science, the Deloro Institute for Advanced Research in Space and Optics, The Veronika A. Rabl Physics Discretionary Fund, Minerva, Yeda-Sela and the Schwartz/Reisman Collaborative Science Program; AGY is the recipient of the Helen and Martin Kimmel Award for Innovative Investigation.

MMK acknowledges generous support from the David and Lucille Packard Foundation.

REFERENCES

- Alard, C., & Lupton, R. H. 1998, *ApJ*, 503, 325, doi: [10.1086/305984](https://doi.org/10.1086/305984)
- Arcavi, I., Gal-Yam, A., Yaron, O., et al. 2011, *ApJL*, 742, L18, doi: [10.1088/2041-8205/742/2/L18](https://doi.org/10.1088/2041-8205/742/2/L18)
- Arcavi, I., Gal-Yam, A., Cenko, S. B., et al. 2012, *ApJL*, 756, L30, doi: [10.1088/2041-8205/756/2/L30](https://doi.org/10.1088/2041-8205/756/2/L30)
- Arcavi, I., Hosseinzadeh, G., Brown, P. J., et al. 2017, *ApJL*, 837, L2, doi: [10.3847/2041-8213/aa5be1](https://doi.org/10.3847/2041-8213/aa5be1)
- Arnett, W. D., Bahcall, J. N., Kirshner, R. P., & Woosley, S. E. 1989, *ARA&A*, 27, 629, doi: [10.1146/annurev.aa.27.090189.003213](https://doi.org/10.1146/annurev.aa.27.090189.003213)
- Bellm, E. 2014, in *The Third Hot-wiring the Transient Universe Workshop*, ed. P. R. Woźniak, M. J. Graham, A. A. Mahabal, & R. Seaman, 27–33
- Bose, S., Valenti, S., Misra, K., et al. 2015, *MNRAS*, 450, 2373, doi: [10.1093/mnras/stv759](https://doi.org/10.1093/mnras/stv759)
- Camp, J., Barthelmy, S., Blackburn, L., et al. 2013, *Experimental Astronomy*, 36, 505, doi: [10.1007/s10686-013-9343-4](https://doi.org/10.1007/s10686-013-9343-4)
- Cao, Y., Kasliwal, M. M., Arcavi, I., et al. 2013, *ApJL*, 775, L7, doi: [10.1088/2041-8205/775/1/L7](https://doi.org/10.1088/2041-8205/775/1/L7)
- Chevalier, R. A. 1976, *ApJ*, 207, 872, doi: [10.1086/154557](https://doi.org/10.1086/154557)
- . 1992, *ApJ*, 394, 599, doi: [10.1086/171612](https://doi.org/10.1086/171612)
- Chevalier, R. A., & Fransson, C. 2008, *ApJL*, 683, L135, doi: [10.1086/591522](https://doi.org/10.1086/591522)
- Colgate, S. A. 1974, *ApJ*, 187, 333, doi: [10.1086/152632](https://doi.org/10.1086/152632)
- Davies, B., Crowther, P. A., & Beasor, E. R. 2018, *MNRAS*, 478, 3138, doi: [10.1093/mnras/sty1302](https://doi.org/10.1093/mnras/sty1302)
- Ensmann, L., & Burrows, A. 1992, *ApJ*, 393, 742, doi: [10.1086/171542](https://doi.org/10.1086/171542)
- Faber, S. M., Phillips, A. C., Kibrick, R. I., et al. 2003, in *Proc. SPIE, Vol. 4841, Instrument Design and Performance for Optical/Infrared Ground-based Telescopes*, ed. M. Iye & A. F. M. Moorwood, 1657–1669
- Falk, S. W. 1978, *ApJL*, 225, L133, doi: [10.1086/182810](https://doi.org/10.1086/182810)
- Filippenko, A. V. 1997, *ARA&A*, 35, 309, doi: [10.1146/annurev.astro.35.1.309](https://doi.org/10.1146/annurev.astro.35.1.309)
- Firth, R. E., Sullivan, M., Gal-Yam, A., et al. 2015, *MNRAS*, 446, 3895, doi: [10.1093/mnras/stu2314](https://doi.org/10.1093/mnras/stu2314)
- Gal-Yam, A. 2017, *Observational and Physical Classification of Supernovae*, 195
- Gal-Yam, A., Kasliwal, M. M., Arcavi, I., et al. 2011, *ApJ*, 736, 159, doi: [10.1088/0004-637X/736/2/159](https://doi.org/10.1088/0004-637X/736/2/159)
- Gandel’Man, G. M., & Frank-Kamenetskii, D. A. 1956, *Soviet Physics Doklady*, 1, 223
- Ganot, N., Gal-Yam, A., Ofek, E. O., et al. 2016, *ApJ*, 820, 57, doi: [10.3847/0004-637X/820/1/57](https://doi.org/10.3847/0004-637X/820/1/57)
- Gezari, S., Dessart, L., Basa, S., et al. 2008, *ApJL*, 683, L131, doi: [10.1086/591647](https://doi.org/10.1086/591647)
- Gezari, S., Rest, A., Huber, M. E., et al. 2010, *ApJL*, 720, L77, doi: [10.1088/2041-8205/720/1/L77](https://doi.org/10.1088/2041-8205/720/1/L77)
- Goldberg, J. A., & Bildsten, L. 2020, arXiv e-prints, arXiv:2005.07290. <https://arxiv.org/abs/2005.07290>
- Grassberg, E. K., Imshennik, V. S., & Nadyozhin, D. K. 1971, *Ap&SS*, 10, 28, doi: [10.1007/BF00654604](https://doi.org/10.1007/BF00654604)
- Higson, E., Handley, W., Hobson, M., & Lasenby, A. 2019, *Statistics and Computing*, 29, 891, doi: [10.1007/s11222-018-9844-0](https://doi.org/10.1007/s11222-018-9844-0)
- Hosseinzadeh, G., Valenti, S., McCully, C., et al. 2018, *ApJ*, 861, 63, doi: [10.3847/1538-4357/aac5f6](https://doi.org/10.3847/1538-4357/aac5f6)
- Ivezić, Ž., Kahn, S. M., Tyson, J. A., et al. 2019, *ApJ*, 873, 111, doi: [10.3847/1538-4357/ab042c](https://doi.org/10.3847/1538-4357/ab042c)
- Katz, B., Sapir, N., & Waxman, E. 2012, *ApJ*, 747, 147, doi: [10.1088/0004-637X/747/2/147](https://doi.org/10.1088/0004-637X/747/2/147)
- Klein, R. I., & Chevalier, R. A. 1978, *ApJL*, 223, L109, doi: [10.1086/182740](https://doi.org/10.1086/182740)
- Kleiser, I. K. W., Poznanski, D., Kasen, D., et al. 2011, *MNRAS*, 415, 372, doi: [10.1111/j.1365-2966.2011.18708.x](https://doi.org/10.1111/j.1365-2966.2011.18708.x)
- Laher, R. R., Surace, J., Grillmair, C. J., et al. 2014, *PASP*, 126, 674, doi: [10.1086/677351](https://doi.org/10.1086/677351)
- Langer, N. 2012, *ARA&A*, 50, 107, doi: [10.1146/annurev-astro-081811-125534](https://doi.org/10.1146/annurev-astro-081811-125534)
- Law, N. M., Kulkarni, S. R., Dekany, R. G., et al. 2009, *PASP*, 121, 1395, doi: [10.1086/648598](https://doi.org/10.1086/648598)
- Martin, D. C., Fanson, J., Schiminovich, D., et al. 2005, *ApJL*, 619, L1, doi: [10.1086/426387](https://doi.org/10.1086/426387)
- Matzner, C. D., & McKee, C. F. 1999, *ApJ*, 510, 379, doi: [10.1086/306571](https://doi.org/10.1086/306571)
- Morrissey, P., Conrow, T., Barlow, T. A., et al. 2007, *ApJS*, 173, 682, doi: [10.1086/520512](https://doi.org/10.1086/520512)
- Nakar, E., & Sari, R. 2010, *ApJ*, 725, 904, doi: [10.1088/0004-637X/725/1/904](https://doi.org/10.1088/0004-637X/725/1/904)
- Ofek, E. O. 2014, *MATLAB package for astronomy and astrophysics*, *Astrophysics Source Code Library*. <http://ascl.net/1407.005>
- Ofek, E. O., & Ben-Ami, S. 2020, *PASP*, 132, 125004, doi: [10.1088/1538-3873/abc14c](https://doi.org/10.1088/1538-3873/abc14c)
- Ofek, E. O., Rabinak, I., Neill, J. D., et al. 2010, *ApJ*, 724, 1396, doi: [10.1088/0004-637X/724/2/1396](https://doi.org/10.1088/0004-637X/724/2/1396)

- Ofek, E. O., Laher, R., Law, N., et al. 2012, *PASP*, 124, 62, doi: [10.1086/664065](https://doi.org/10.1086/664065)
- Oke, J. B., Cohen, J. G., Carr, M., et al. 1995, *PASP*, 107, 375, doi: [10.1086/133562](https://doi.org/10.1086/133562)
- Pastorello, A., Baron, E., Branch, D., et al. 2005, *MNRAS*, 360, 950, doi: [10.1111/j.1365-2966.2005.09079.x](https://doi.org/10.1111/j.1365-2966.2005.09079.x)
- Rabinak, I., & Waxman, E. 2011, *ApJ*, 728, 63, doi: [10.1088/0004-637X/728/1/63](https://doi.org/10.1088/0004-637X/728/1/63)
- Rau, A., Kulkarni, S. R., Law, N. M., et al. 2009, *PASP*, 121, 1334, doi: [10.1086/605911](https://doi.org/10.1086/605911)
- Rubin, A., & Gal-Yam, A. 2017, *ApJ*, 848, 8, doi: [10.3847/1538-4357/aa8465](https://doi.org/10.3847/1538-4357/aa8465)
- Rubin, A., Gal-Yam, A., De Cia, A., et al. 2016, *ApJ*, 820, 33, doi: [10.3847/0004-637X/820/1/33](https://doi.org/10.3847/0004-637X/820/1/33)
- Sagiv, I., Gal-Yam, A., Ofek, E. O., et al. 2014, *AJ*, 147, 79, doi: [10.1088/0004-6256/147/4/79](https://doi.org/10.1088/0004-6256/147/4/79)
- Sakurai, A. 1960, *Communications on Pure and Applied Mathematics*, 13, 353, doi: [10.1002/cpa.3160130303](https://doi.org/10.1002/cpa.3160130303)
- Sapir, N., Katz, B., & Waxman, E. 2011, *ApJ*, 742, 36, doi: [10.1088/0004-637X/742/1/36](https://doi.org/10.1088/0004-637X/742/1/36)
- . 2013, *ApJ*, 774, 79, doi: [10.1088/0004-637X/774/1/79](https://doi.org/10.1088/0004-637X/774/1/79)
- Sapir, N., & Waxman, E. 2017, *ApJ*, 838, 130, doi: [10.3847/1538-4357/aa64df](https://doi.org/10.3847/1538-4357/aa64df)
- Schawinski, K., Justham, S., Wolf, C., et al. 2008, *Science*, 321, 223, doi: [10.1126/science.1160456](https://doi.org/10.1126/science.1160456)
- Schlegel, D. J., Finkbeiner, D. P., & Davis, M. 1998, *ApJ*, 500, 525, doi: [10.1086/305772](https://doi.org/10.1086/305772)
- Schmidt, B. P., Kirshner, R. P., Eastman, R. G., et al. 1993, *Nature*, 364, 600, doi: [10.1038/364600a0](https://doi.org/10.1038/364600a0)
- Shappee, B., Prieto, J., Stanek, K. Z., et al. 2014, in *American Astronomical Society Meeting Abstracts*, Vol. 223, *American Astronomical Society Meeting Abstracts #223*, 236.03
- Skilling, J. 2004, in *American Institute of Physics Conference Series*, Vol. 735, *American Institute of Physics Conference Series*, ed. R. Fischer, R. Preuss, & U. V. Toussaint, 395–405
- Skilling, J. 2006, in *American Institute of Physics Conference Series*, Vol. 872, *Bayesian Inference and Maximum Entropy Methods In Science and Engineering*, ed. A. Mohammad-Djafari, 321–330
- Smartt, S. J. 2015, *PASA*, 32, e016, doi: [10.1017/pasa.2015.17](https://doi.org/10.1017/pasa.2015.17)
- Smartt, S. J., Eldridge, J. J., Crockett, R. M., & Maund, J. R. 2009, *MNRAS*, 395, 1409, doi: [10.1111/j.1365-2966.2009.14506.x](https://doi.org/10.1111/j.1365-2966.2009.14506.x)
- Soderberg, A. M., Berger, E., Page, K. L., et al. 2008, *Nature*, 453, 469, doi: [10.1038/nature06997](https://doi.org/10.1038/nature06997)
- Soumagnac, M. T., Ofek, E. O., Gal-yam, A., et al. 2019, *ApJ*, 872, 141, doi: [10.3847/1538-4357/aafe84](https://doi.org/10.3847/1538-4357/aafe84)
- Soumagnac, M. T., Ganot, N., Irani, I., et al. 2020, *ApJ*, 902, 6, doi: [10.3847/1538-4357/abb247](https://doi.org/10.3847/1538-4357/abb247)
- Speagle, J. S. 2020, *MNRAS*, 493, 3132, doi: [10.1093/mnras/staa278](https://doi.org/10.1093/mnras/staa278)
- Sullivan, M., Howell, D. A., Perrett, K., et al. 2006, *AJ*, 131, 960, doi: [10.1086/499302](https://doi.org/10.1086/499302)
- Taddia, F., Sollerman, J., Leloudas, G., et al. 2015, *A&A*, 574, A60, doi: [10.1051/0004-6361/201423915](https://doi.org/10.1051/0004-6361/201423915)
- Tonry, J. L., Denneau, L., Heinze, A. N., et al. 2018, *PASP*, 130, 064505, doi: [10.1088/1538-3873/aabadf](https://doi.org/10.1088/1538-3873/aabadf)
- Valenti, S., Sand, D., Pastorello, A., et al. 2014, *MNRAS*, 438, L101, doi: [10.1093/mnras/ltt171](https://doi.org/10.1093/mnras/ltt171)
- Yaron, O., & Gal-Yam, A. 2012, *PASP*, 124, 668, doi: [10.1086/666656](https://doi.org/10.1086/666656)